University of Science and Technology of Hanoi

Space Science and Spacecraft technology department

INTERNSHIP REPORT IFIRSE, ICISE – Neutrino Group
MASTER 1 SPACE
01-07-2023 – 01-09-2023

SIMULATION AND MACHINE LEARNING FOR PARTICLE IDENTIFICATION WITH WATER CHERENKOV NEUTRINO DETECTOR

By :

Milo Charavet – E22.M1.SA.002

Supervisor :

Dr. Cao Van Son

Table of Contents

Acknowledgements

First of all, I would like to thank the University of Science and Technology of Hanoi for having placed their trust in me. The attentiveness and support I received enabled me to quickly find an internship, with the aim of refining my professional project.

I'd also like to thank Dr. Jean Tran Thanh Van, IFIRSE, ICISE Director, who believed in my potential and welcomed me into the institute.

I would also like to extend a special thank you to Dr. Son Cao, who supported and advised me, and above all passed on his expertise in the neutrino field. The advice from him during all the internship and from the entire Neutrino Group during the meetings we had each Friday really helped to move forward each week.

This internship has enabled me to refine certain aspects of my career project and is the culmination of my first master year.

As a closing remark, I really would like to express my appreciation and gratitude to the Vietnamese students, organizers and lecturers of the Vietnam Summer School of Neutrino, the other students who participated and enjoyed as much as I did this 7th VSoN, and ICISE staff. The first chapters of this report are the result of my readings, but also the courses provided by the lecturers who introduced us to the world of experimental neutrino physics.

Chapter 1

Introduction

Internship and Neutrino Group

Since the discovery of atmospheric neutrino oscillations by the Super-Kamiokande (SK) detector in 1998, our understanding of the properties of neutrinos has grown dramatically. The study of neutrinos, which have an extremely low mass compared to other elementary particles, gives us the possibility to discover new physics beyond the Standard Model and therefore, has attracted a great deal of attention in modern particle physics.

This is particularly true for the Neutrino Group, which belongs to the Institute For Interdisciplinary Research in Science and Education (IFIRSE). The Neutrino Group has grown up at the International Center for Interdisciplinary Science and Education (ICISE), placed in the coastal city named Quy Nhon, Vietnam, under the lead of Prof. Tsuyoshi Nakaya, Kyoto University, who is now the spokesperson of both T2K and Hyper-K experiments. "*In the early stage, the group might focus on data and Monte Carlo (MC) simulation analysis. For a longer term, the group would be expanded and a possibility to build the R&D laboratory as well as real detectors placed at ICISE. The intermediate goal is until 2026, when the next generation of the long-baseline neutrino experiments, Hyper-K and DUNE, come to operate, our Vietnamese group can join directly these experiments as a strong group.*" [1]

I therefore chose to do my internship at the Neutrino Group, IFIRSE/ICISE. This choice of internship is motivated by my wish to continue my learning and research in particle physics and more precisely, in neutrino physics, which is of particular interest to me both from a very concrete point of view, due to the challenge their detection represents, and from the point of view of the fundamental scientific questions that remain open in this field. Neutrinos are at the frontier between the known Standard Model and the physics that may lie beyond it. Indeed, their mass acquisition mechanism and their Dirac or Majorana nature are still unknown. What's more, this field of research has numerous connections with other themes: the matter/antimatter asymmetry of the universe could have its origin in CP violation in the neutrino sector; high-energy neutrinos emitted by

astrophysical sources enable their study, ... So, first and foremost, I wanted to learn and train myself on neutrino detection and measurement techniques.

The aim of this internship was, then, firstly, to become familiar with the simulation and reconstruction of events from the Super-Kamiokande detector and, secondly, to develop and apply the skills needed to identify and classify these different events. My internship focused on the following points:

- use the WCSim package from the Geant4 software to simulate the signal pattern (Cherenkov rings formed by the passage of charged particles like muons and electrons) in Water Cherenkov detectors such as Super-Kamiokande or under-construction Hyper- Kamiokande

- learn how to display events

- learn how to distinguish muon-like events (from muon neutrino interactions) and electron-like events (from electron neutrino interactions)

- learn machine learning algorithm for classifying muon-like events from electron-like events

- understand the physics potentials of Hyper-Kamiokande experiments

In my internship, I mostly alternated working on the simulation part and reading papers on the classification algorithms I could use. The first two weeks were devoted to the first simulations of the Water Cherenkov detector and also to the first performance tests of the classification algorithms for particles. The following two weeks were devoted to the Vietnam Summer School of Neutrino, during which physicists from Vietnam, Japan, India, ... came to the ICISE to introduce us, student from all over the world, to the field of neutrino experimental physics. Finally, during the last month, I coded, tested and applied the machine learning algorithm used for the classification. During the two months, I was in contact with the other members of the Neutrino Group on site, and the meetings with the other members every Friday to discuss the progress of our research were a great help.

Context

For almost 20 years, the Standard Model of elementary particle physics, comprising quantum chromodynamics and the Glashow-Weinberg-Salam theory of electroweak processes, has been accepted as the theory that describes all elementary interactions except gravity. There have been no convincing experimental findings that require a modification of the current Standard Model. The discovery of the Higgs boson (H), the origin of mass [2], in the ATLAS and CMS experiments at the Large Hadron Collider (LHC) of the European Organization for Nuclear Research (CERN) in 2012 confirmed the existence of all particles represented in the current Standard Model of elementary particles (Figure 1.1).

	1st generation	2nd generation	3rd generation
Quarks	up (u), down (d)	charm (c), strange (s)	top (t), bottom (b)
Leptons	electron (e), e-neutrino (ν_e)	muon (μ), e-neutrino (ν_μ)	tau (τ), e-neutrino (ν_τ)
Gauge bosons	photon (γ), weak boson ($Z^0, W^\pm$), gluon (g)		
Scalar bosons	Higgs (H^0)		

Figure 1.1: Elementary particles in the Standard Model

Some questions remain unanswered, such as the nature of dark matter, the whereabouts of antimatter after the Big Bang, the three generations of quarks and leptons, and the differences in mass scales between generations. One of these is the nature of neutrinos, for which physics beyond the Standard Model is needed. Moreover, another connection needs to be mentioned.

When the Nobel Foundation awarded the 2002 Nobel Prize in Physics to Ray Davis and Masatoshi Koshiba, it could have chosen to highlight any one of their many achievements. R. Davis had become famous for detecting neutrinos from the Sun, the first extraterrestrial examples of these elusive particles; Dr. Koshiba had detected others from the great supernova explosion of 1987. Their work helped establish that neutrinos, thought by physicists to have zero mass, in fact had a small mass. But the Nobel Foundation honored

R. Davis and M. Koshiba above all for having inaugurated a new scientific discipline: neutrino astrophysics.

Neutrino astrophysics is the branch of astrophysics that observes celestial objects using detectors of neutrinos, low-mass neutral leptons described by electroweak theory. Given their very weak interaction with matter, neutrinos have the ability to cross cosmological distances without deviating from their initial trajectory, making them excellent astronomical messengers that can be directly traced back to their place of production.

Observing cosmic neutrinos enables us to better study the workings of the most energetic and distant phenomena in the Universe. However, the difficulty of detecting these particles currently limits our ability to detect celestial objects emitting neutrinos. Before 2022, only three associations of neutrinos with celestial objects had been established: the Sun, supernova 1987A, and the active galaxy TXS0506+056.

The first experiments to observe solar neutrinos were carried out in 1967 – 1968 by scientists Raymond Davis Jr. and John N. Bahcall in the Homestake experiment [3]. A neutrino detector, set up underground at a depth of 1,480 m to block the cosmic ray background and containing 610 tons of liquid perchloroethylene (C_2Cl_4), was used at Brookhaven National Laboratory continuously from 1968 to 1973. Researchers soon noticed that the number of neutrinos detected was lower than predicted by theory[1].

In July 2018, the IceCube observatory announced that it had been able to determine the origin of a high-energy neutrino in the TXS0506+056 blazar, located 3.7 billion light-years from Earth. This is the first detection to locate an object in the sky, and the first source of cosmic neutrinos to be identified [4].

In November 2022, IceCube made another important neutrino detection, identifying 79 neutrinos from the M77 galaxy, just 47 million light-years away. This first detection in a little distant and much-studied object should serve as a benchmark for future observations, and enable us to learn more about the active core of this galaxy.

In the next chapter, we describe the properties of neutrinos, which are the main target of SK’s and HK's observations. An overview of the physics that HK aims for is given in Appendix A.

[1] This can be explained by the adiabatic flavor conversion of neutrinos in the matter of the Sun which is somehow different from the neutrino oscillation [A. Yu. Smirnov, *Solar neutrinos: Oscillations or No-oscillations?*, 2017]

Chapter 2

Neutrino Physics

Overview

In the previous section, we mentioned neutrinos as elementary particles with properties that are not explained by the Standard Model, which describes the elementary particle world almost completely. In the Standard Model, neutrinos are leptons with no electric charge and only weak interactions and gravitational interactions. They have no mass, are left-handed, and have three generations depending on the charged lepton (e, μ, τ), and the number of leptons in each generation is conserved.

Neutrinos were first proposed as unknown neutral particles by W. Pauli in 1930 to explain the fact that the kinetic energy spectrum of electrons emitted in nuclear beta decay is a continuous spectrum [5]. In 1954, Reines and Cowan succeeded in directly detecting antielectron neutrinos from nuclear reactors using a 300-liter liquid scintillator, establishing experimentally the existence of neutrinos [6]. In 1962, the μ neutrino was discovered, and in 1997, the τ neutrino was discovered. Thus far, experiments have confirmed the existence of three generations of neutrinos and the existence of various neutrino sources in nature. In the Standard Model, neutrinos were thought to be massless, but the discovery of neutrino oscillations in SK in 1998 [7] strongly suggested that neutrinos have finite masses. The HK experiment, scheduled to begin in 2027, will be able to study neutrinos with large statistics. Below, we discuss the properties of neutrinos, and more precisely neutrino oscillation, which is the focus of much attention in the search for theories beyond the Standard Model.

Neutrino Oscillation

Neutrinos, which have no charge and react only through weak interactions, are known to have three flavor eigenstates: ν_e, ν_μ, ν_τ, and they take these eigenstates when they react

through weak interactions. On the other hand, mass eigenstates are different from flavor eigenstates, and quantum mixing between mass eigenstates $|\nu_i\rangle (i = 1,2,3)$ and flavor eigenstates $|\nu_\alpha\rangle (\alpha = e, \mu, \tau)$ is a Pontecorvo-Maki-Nakagawa-Sakata (PMNS) matrix as follows.

$$|\nu_\alpha\rangle = \sum_i U_{\alpha i} |\nu_i\rangle \qquad (\alpha = e, \mu, \tau) \tag{1.1}$$

The PMNS mixing matrix U is a 3×3 unitary matrix and is represented by the three mixing angles θ_{12}, θ_{13}, and θ_{23}, the CP symmetry breaking parameters δ_{CP}, and the Majorana CP phases α_1 and α_2 as follows [8].

$$U = \begin{pmatrix} U_{e1} & U_{e2} & U_{e3} \\ U_{\mu 1} & U_{\mu 2} & U_{\mu 3} \\ U_{\tau 1} & U_{\tau 2} & U_{\tau 3} \end{pmatrix} \tag{1.2}$$

$$= \begin{pmatrix} 1 & 0 & 0 \\ 0 & c_{23} & s_{23} \\ 0 & -s_{23} & c_{23} \end{pmatrix} \begin{pmatrix} c_{13} & 0 & s_{13} e^{-i\delta_{CP}} \\ 0 & 1 & 0 \\ -s_{13} e^{i\delta_{CP}} & 0 & c_{13} \end{pmatrix} \begin{pmatrix} c_{12} & s_{12} & 0 \\ -s_{12} & c_{12} & 0 \\ 0 & 0 & 1 \end{pmatrix} \begin{pmatrix} e^{-i\alpha_1/2} & 0 & 0 \\ 0 & e^{i\alpha_1/2} & 0 \\ 0 & 0 & 1 \end{pmatrix}$$

where $c_{ij} \equiv \cos\theta_{ij}$ and $s_{ij} \equiv \sin\theta_{ij}$. δ_{CP}, α_1 and α_2 are the CP-symmetry breaking phases. α_1 and α_2 take non-zero values when the neutrino is a Majorana particle[2]. Also, since the antineutrino mixing is represented by the complex conjugate U^*, if δ_{CP} is non-zero or non-π, then the PMNS mixing matrix is no longer a real matrix, predicting CP symmetry breaking in the leptons.

The last terms, α_1 and α_2, are called the Majorana phases, which exist if the neutrino is a Majorana particle, but they do not contribute to neutrino oscillations. Whether neutrinos are Majorana particles or not is a very important question, and experimental verification is in progress through searches for neutrino-less double beta decays. In Japan, the KamLAND-Zen experiment has produced the world's most sensitive search results [9], and other experimental projects are underway, but we will not discuss them here, since the main focus is on neutrino oscillations.

[2] fermion which is its own antiparticle

2.2.1 Neutrino oscillation in vacuum

When neutrinos are produced through weak interaction reactions, they react as flavor eigenstates, but when they propagate from the production point to the observation point, they evolve in time according to mass eigenstates, which can cause a phenomenon called neutrino oscillation, in which the neutrino flavor changes between the production and observation times. A neutrino produced at time $t = 0$ in the flavor eigenstate $|\nu_\alpha\rangle$ has mass eigenstate as in Equation 1.1.

$$|\nu(t=0)\rangle = |\nu_\alpha\rangle = \sum_i U_{\alpha i}|\nu_i\rangle \tag{1.3.1}$$

If the momentum of the neutrino is p_i and the mass of the mass eigenstate $|\nu_i\rangle$ is m_i, the energy can be written as $E_i = \sqrt{{p_i}^2 + {m_i}^2}$, and assuming that $|\nu\rangle$ is a plane wave, then $|\nu_i(t)\rangle = e^{-iE_i t}|\nu_i(0)\rangle$. At time t, having traveled a distance L ($L \sim$ constant for relativistic neutrinos), the state is expressed as follows.

$$|\nu(t)\rangle = \sum_i U_{\alpha i} e^{-iE_i t}|\nu_i\rangle \tag{1.3.2}$$

The probability that this neutrino is observed at time t as a flavor eigenstate $|\nu_\beta\rangle$ is:

$$P(\nu_\alpha \to \nu_\beta) = \left|\langle \nu_\beta|\nu(t)\rangle\right|^2 = \left|\sum_i U_{\alpha i} e^{-iE_i t} U^*_{\beta i}\right|^2 \tag{1.3.3}$$
$$= \sum_i \sum_j U_{\alpha i} U_{\beta j}\, U^*_{\beta i} U^*_{\alpha j} e^{-i(E_i - E_j)t}$$

Assuming $p_i \approx p_j \equiv p \approx E$ ($p \gg m_i$) in relativistic neutrinos, the energy E_i can be approximated as:

$$E_i = \sqrt{{p_i}^2 + {m_i}^2} \approx p + \frac{{m_i}^2}{2E} \tag{1.3.4}$$

and we can consider $E_i \approx E_j = p$:

$$E_i - E_j \approx \frac{{m_i}^2 - {m_j}^2}{2E} \equiv \frac{{\Delta m_{ij}}^2}{2E} \tag{1.3.5}$$

The distance traveled by the neutrino at time t is L. The distance traveled at time t by a neutrino traveling at nearly the speed of light is L. Given the orthogonality $\langle \nu_j | \nu_i \rangle = \delta_{ij}$ of the mass eigenstates, the oscillation probability $P(\nu_\alpha \to \nu_\beta)$ becomes:

$$P(\nu_\alpha \to \nu_\beta) = \sum_i \sum_j U_{\alpha i} U_{\beta j}\, U^*_{\beta i} U^*_{\alpha j} \exp\left\{\frac{-i\Delta {m_{ij}}^2 L}{2E}\right\} \tag{1.3.6}$$

$$= \delta_{\alpha\beta} - 4\sum_{i>j} Re\left(U_{\alpha i} U_{\beta j} U^*_{\beta i} U^*_{\alpha j}\right) \sin^2 \frac{\Delta {m_{ij}}^2 L}{4E} + 2\sum_{i>j} Im\left(U_{\alpha i} U_{\beta j} U^*_{\beta i} U^*_{\alpha j}\right) \sin^2 \frac{\Delta {m_{ij}}^2 L}{2E}$$

From this, it can be seen that when neutrinos have different masses ($\Delta {m_{ij}}^2 \neq 0$), flavor oscillations occur and the oscillation probability depends on the ratio L/E between the neutrino energy E and the distance L travelled. Thus, observations of neutrino oscillations in the vacuum provide evidence of neutrino mass. Due to the fact that, in many cases, oscillations between two neutrino generations are significantly observed, we will only consider mixing between two neutrino generations as an approximation. In this case, the mixing corresponding to Eq. 1.3.1 can be expressed using the mixing angle θ of the mass eigenstate.

$$\begin{pmatrix} \nu_\alpha \\ \nu_\beta \end{pmatrix} = \begin{pmatrix} \cos\theta & \sin\theta \\ -\sin\theta & \cos\theta \end{pmatrix} \begin{pmatrix} \nu_1 \\ \nu_2 \end{pmatrix} \tag{1.3.7}$$

The oscillation probability $P(\nu_\alpha \to \nu_\beta)$ of a flavor is:

$$P(\nu_\alpha \to \nu_\beta) = \begin{cases} \sin^2 2\theta \sin^2 \dfrac{\Delta {m_{ij}}^2 L}{4E}, & (\alpha \neq \beta) \\ 1 - \sin^2 2\theta \sin^2 \dfrac{\Delta {m_{ij}}^2 L}{4E}, & (\alpha = \beta) \end{cases} \tag{1.3.8}$$

where $\Delta m^2 \equiv {m_2}^2 - {m_1}^2$. Again, the oscillation probability depends on L/E, and the phase of the part containing L/E can be written:

$$\frac{\Delta m^2 L}{4E} = \frac{\Delta m^2\ [eV^2]\,.\,L[m]}{4E\ [eV]} \times \frac{\hbar c}{197\ [MeV.fm]} \approx \frac{1.267\ \Delta m^2\ [eV^2]\,.\,L[m]}{E\ [GeV]} \tag{1.3.9}$$

From this relationship, if we know the distance to the neutrino source, the neutrino energy, and the neutrino flux to be observed by the detector, we can determine the squared difference in neutrino mass from the number of detections. The existence of neutrino oscillations is proved by the fact that the number of atmospheric neutrinos ν_μ differs between those that have passed through the earth and those that have not, which also explains the deviation of ν_e from the predicted value for solar neutrinos.

2.2.2 Neutrino oscillation in matter

Neutrinos propagating in dense media rarely interact with electrons, protons, or neutrons in the medium. For protons and neutrons, all neutrinos undergo neutral-current reactions via the Z boson. For electrons, on the other hand, neutral-current reactions mediated by the Z boson occur regardless of neutrino flavor, while charged-current reactions mediated by the W boson occur only in electron neutrinos. This difference in the propagation of electron neutrinos through matter due to differences in the way they interact is called the matter effect. Considering the effect of the potential felt by neutrinos due to resonant scattering of neutrinos with electrons in matter, it can be interpreted that the potential V_{CC} is added only to electron neutrinos.

$$V_{CC} = \pm\sqrt{2}G_F n_e \tag{1.4}$$

where G_F is the Fermi coupling constant and n_e is the electron number density in matter, corresponding to a positive sign for neutrinos and a negative sign for antineutrinos. V_{CC}~10^{13} eV for the Earth's core (n_e~$10\ \mathrm{g/cm^3}$) and V_{CC}~10^{12} eV for the Sun's core (n_e~$100\ \mathrm{g/cm^3}$).

The oscillation probabilities of second-generation neutrinos under this potential are obtained by replacing θ and Δm^2 in Eq. 1.2.10 with the following θ_M and $\Delta {m_M}^2$.

$$\sin^2 2\theta_M = \frac{\sin^2 2\theta}{\sin^2 2\theta + (\Gamma - \cos 2\theta)^2} \tag{1.5}$$

$$\Delta {m_M}^2 = \Delta m^2 \sqrt{\sin^2 2\theta + (\Gamma - \cos 2\theta)^2} \tag{1.6}$$

where $\Gamma \equiv 2\sqrt{2}G_F n_e E/\Delta m^2$. Due to this material effect, even for vibration modes with small θ, the resonance condition. The oscillation probability can be large at neutrino

energies such that $\Gamma = \cos 2\theta$ is satisfied. This resonance is also known as the Δm^2. Since the resonance depends on the sign of Δm^2, it is possible to determine the neutrino mass ordering from the observation of resonance oscillations due to the matter effect.

2.2.3 Neutrino oscillation parameters

As can be seen from Equations 1.2.8 and 1.2.10, the neutrino oscillation probability depends on $\Delta {m_{ij}}^2 - E/L$, so for a given energy and baseline there are six independent parameters describing neutrino oscillations: three mixing angles, one CP phase and two mass-squared differences. Measurements of the oscillation parameters have been made using multiple neutrino sources over a wide energy range. Among the oscillation parameters, θ_{12} and $\Delta {m_{21}}^2$ are mainly measured by observations of solar neutrinos from fusion reactions in the Sun and reactor neutrinos from fission reactions in nuclear reactors, θ_{13} is measured by observations of artificially produced accelerator neutrinos from hadron decay using accelerators and reactor neutrinos, θ_{23}, $\Delta {m_{32}}^2$, and δ_{CP} have been measured by observations of atmospheric neutrinos and accelerator neutrinos, respectively. In particular, the 2-3 intergenerational θ_{23} has been suggested to be almost maximally mixed ($\theta_{23} \approx 45°$), and whether it is exactly 45° is one of the subjects of future neutrino physics to demonstrate any symmetry in tau and mu neutrinos distribution.

Table 1.1 shows the results of the current measurements of the oscillation parameters obtained from the various measurements. Most parameters are measured with an accuracy of a few percent, but the mass ordering, δ_{CP}, and θ_{23} octant (lower octant if $\theta_{23} < 45°$ or higher if $\theta_{23} > 45°$) are currently open problems for the oscillation parameters (see Appendix A for more precision).

Parameter	**Best-fit values**	**3σ ranges**	**Relative 1σ precision (in present)**
Δm^2_{21} (eV^2)	7.5×10^{-5}	$[7.0, 8.1] \times 10^{-5}$	$\sigma\,(\Delta m^2_{21}) = 2.4\%$
Δm^2_{31} (eV^2)	2.46×10^{-3} (NH)	$[2.32, 2.61] \times 10^{-3}$ (NH)	$\sigma\,(\Delta m^2_{31}) = 2.0\%$
Δm^2_{32} (eV^2)	-2.45×10^{-3} (IH)	$-[2.59, 2.31] \times 10^{-3}$ (IH)	$\sigma\,(\Delta m^2_{32}) = 1.9\%$
$\sin^2\theta_{12}$	0.3	[0.27, 0.34]	$\sigma\,(\Delta \sin^2\theta_{12}) = 4.4\%$
$\sin^2\theta_{23}$	0.45 (NH), 0.58 (IH)	[0.38, 0.64]	$\sigma\,(\Delta \sin^2\theta_{23}) = 8.7\%$
$\sin^2\theta_{13}$	0.022	[0.018, 0.025]	$\sigma\,(\Delta \sin^2\theta_{13}) = 5.3\%$
δ_{CP} (°)	306	[0, 360]	-

Table 1.2: Measured results of vibration parameters [10]

Atmospheric neutrino

For the analysis of atmospheric neutrinos, it is essential to develop reliable models of their production mechanism. These have to provide quantitative predictions of flux, spectra and flavor composition of atmospheric neutrinos at the detector site.

Atmospheric neutrinos are produced by cosmic rays that produce secondary particles in the atmosphere, as shown in Figure 1.1. Some of the sources are presented in Appendix A. Primary cosmic rays entering the atmosphere interact with atomic nuclei in the atmosphere to produce secondary cosmic rays such as π and K. Atmospheric neutrinos are produced by the decay of these secondary cosmic rays. The decay process is as follows.

$$\pi^+, K^+ \rightarrow \mu^+ + \nu_\mu \tag{1.7}$$
$$\mu^+ \rightarrow e^- + \nu_e + \overline{\nu_\mu} \tag{1.8}$$
$$\pi^-, K^- \rightarrow \mu^- + \overline{\nu_\mu} \tag{1.9}$$
$$\mu^- \rightarrow e^- + \nu_\mu + \overline{\nu_e} \tag{1.10}$$

Overall, two ν_μ and one ν_e are created by the decay of π and K. The flux ratio of $(\nu_\mu + \overline{\nu_\mu})/(\nu_e + \overline{\nu_e})$, $R(\mu/e)$ is expected to be 2 with an indefinite value of less than 5% in the low energy region.

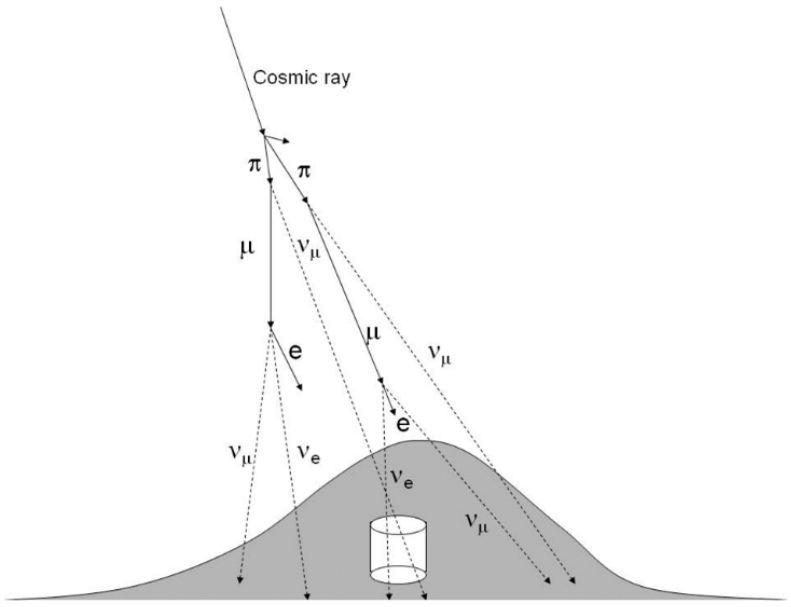

Figure 1.1: Collisions between cosmic rays and atmospheric nuclei [11]

However, these ratios depend on the energy of the neutrinos. For high energies, $R(\mu/e)$ is larger than 2, because the muons are highly relativistic and many of them do not decay on their way to the detector, which means that no ν_e is created.

Theoretical calculations of atmospheric neutrino fluxes have been performed by independent groups such as Honda [12], Fluka [13], Bartol [14], and others (Super Kamiokande mainly uses the Honda flux in its analysis). Comparisons with other fluxes are also made in order to estimate the phylogenetic uncertainties arising from the theoretical calculations. Figure 2.2 shows the results of four calculations for the Kamioka site.

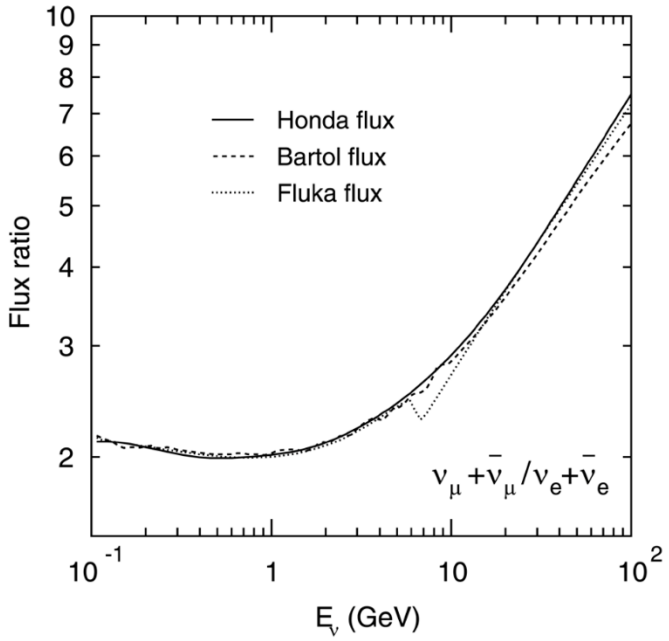

Figure 1.2: Calculations of the neutrino flux ratio $R(\mu/e)$ to atmospheric neutrino energy by the three groups [10]. The solid line is by Honda, the wavy line by Bartol, and the dotted line by Fluka.

This deficit, which might be caused by the neutrino oscillation, encourages research in atmospheric neutrinos for the discovery of non-standard physics. New measurements on the properties and behavior of ν_μ and ν_e will help to clarify the situation. But before this analysis, an identification of the particle produced by neutrino interaction should be performed. This is the main point of my internship. Indeed, the open problems mentioned in the previous chapter are very challenging and require large samples of neutrino events, which correlates with the development of the Super-Kamiokande and Hyper-Kamiokande experiment. During this internship, I also wanted to learn how machine learning can help to prevent important data loss and accurately identify the class of neutrino events.

Chapter 3

Super-Kamiokande Description

Overview

Super-Kamiokande is a large water Cherenkov instrument located in Kamioka-cho, Hida City, Gifu Prefecture [15]. The detector consists of a cylindrical stainless steel tank with a diameter of 39.3 m and a height of 41.4 m, and a number of photomultiplier tubes mounted inside.

The water tank consists of two layers, and the inner and outer tanks are separated by a light-shielding structure. More than 11,000 photomultiplier tubes with a diameter of 50 cm are mounted inward on the wall of the inner tank. The outer tank is mainly used to identify particles entering from outside, such as cosmic ray muons, and has more than 1,800 photomultiplier tubes with a diameter of 20 cm mounted facing outward. These photomultiplier tubes capture the weak light called Cherenkov light emitted by charged particles in the water to observe neutrinos and other particles. The effective mass of the tank is about 22,500 tons, because many data analyses require that the reaction point of an event be at least 2 m away from the inner wall.

On top of and around the tank are electronic circuits for processing the electrical signals from the photomultiplier tubes, a group of devices for calibration, and equipment for purifying ultrapure water. Since the equipment is in operation 24 hours a day, collaborating researchers monitor the equipment in three shifts of eight hours each. Currently, the daytime shift is monitored in the control room in the mine, which is located right next to the detector, and the nighttime shift is monitored in a nearby facility.

A Helmholtz coil is wound around the outer circumference of the Super-Kamiokande tank to cancel the geomagnetic field. Photomultiplier tubes are susceptible to magnetic fields because the orbits of electrons are bent, but the distance from the photocathode to the dynode is long for large-diameter photomultiplier tubes, so even geomagnetism has an effect.

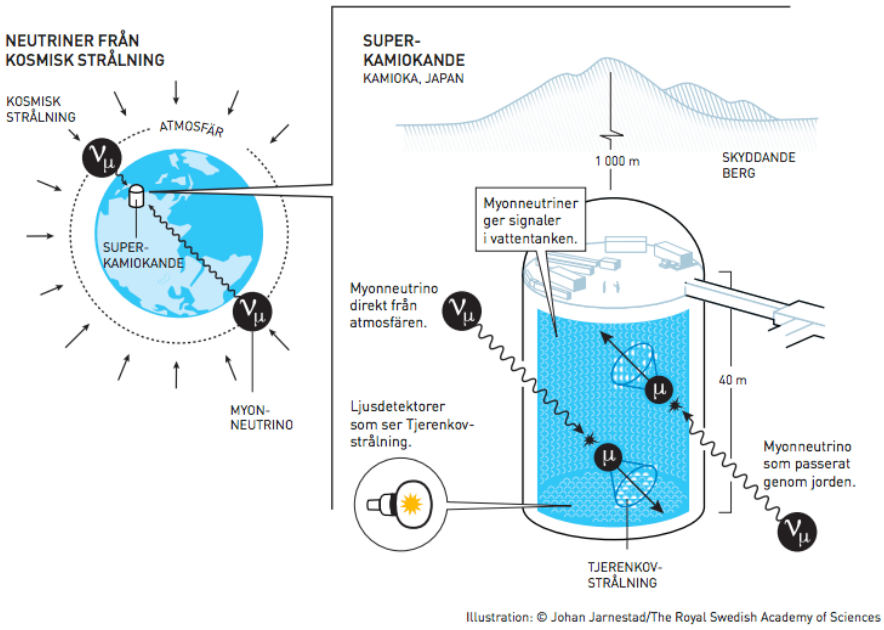

Figure 2.1 : Schematic of Super-Kamiokande detector

Detection principle

Neutrino detection in SK is based on the detection of Cherenkov radiation. Neutrinos are highly transmissive particles with a very small reaction cross-section because they have no charge and only weak interactions. However, in rare cases, neutrinos react with nucleons and electrons in ultrapure water in the detector to produce charged particles. These charged particles fly at almost the speed of light and emit Cherenkov light. The neutrino is observed by capturing this Cherenkov light with a photodetector.

3.2.1 Neutrino reaction

There are two types of weak interactions that occur with neutrinos: charged-current (CC) reactions and neutral current (NC) reactions. In the CC reaction, charge is exchanged between the reacting particles via the $W^{\pm}$ boson. The leptons produced in the CC reaction are of the same generation as the neutrino flavor before the reaction, so it is possible to identify the neutrino flavor that caused the reaction. However, since the CC reaction

requires energy to produce electrons and muons, there is a lower limit to the neutrino energy at which the reaction can take place. On the other hand, the NC reaction is mediated by the Z^0 boson. In this case, no charge is transferred, and the neutrino only transfers some energy to the reacting target.
The neutrino only transfers some of its energy to the reacting target. Therefore, it is not possible to identify the neutrino flavor from the charged particles after the reaction. Examples of specific interactions are listed below. Examples of interactions are listed below.

Charged current reaction

- Quasi-elastic scattering $\nu_l + n \rightarrow l + p, \overline{\nu_l} + p \rightarrow \bar{l} + n$
- Deep inelastic scattering $\nu + N \rightarrow lepton + N' + hadrons$
- Single-pion generation $\nu + N \rightarrow lepton + N' + \pi$
- Multi-pion generation $\nu + N \rightarrow lepton + N' + m\pi$
- Coherent-pion generation $\nu + {}^{16}\mathrm{O} \rightarrow lepton^{\pm} + \pi^{\pm} + {}^{16}\mathrm{O}$

Neutral current reaction

- Quasi-elastic scattering $\nu + N \rightarrow \nu + N'$
- Deep inelastic scattering $\nu + N \rightarrow \nu + N' + hadrons$
- Single-pion generation $\nu + N \rightarrow \nu + N' + \pi$
- Multi-pion generation $\nu + N \rightarrow \nu + N' + m\pi$
- Coherent-pion generation $\nu + {}^{16}\mathrm{O} \rightarrow \nu + \pi^0 + {}^{16}\mathrm{O}$

In electron-targeted scattering and the relatively high-energy CC reaction, the scattered leptons have information on the direction of arrival of the neutrino. Therefore, in such events, the reconstructed information can be used to search for neutrinos from supernova explosions with directional sensitivity to the source. In the case of NC reactions, it is possible to detect Cherenkov radiation from hadrons such as pions in the final state.

3.2.2 Event reconstruction in Water Cherenkov photodetectors

Cherenkov radiation is a phenomenon in which charged particles radiate electromagnetic waves into matter. The speed of light in a material is slower than the speed of light c in a vacuum, and if the refractive index of the material is n, the speed of light propagation in

the material is c/n. Therefore, charged particles can move faster than the speed of light in matter and emit light called Cherenkov light. Figure 2.2 shows the Cherenkov radiation, which is emitted in the form of a cone. The radiation angle θ of the cone is determined by the velocity of the parent particle to satisfy the laws of conservation of momentum and energy. The relation between velocity β and radiation angle θ is as follows.

$$\cos\theta = \frac{1}{\beta n} \tag{3.1}$$

Also, the number of Cherenkov radiation emitted per unit length by a particle of charge ze (where e is elementary charge) at wavelengths λ to $\lambda + d\lambda$, $dN(\lambda)$ is:

$$dN(\lambda) = 2\pi\alpha z^2 \left\{1 - \left(\frac{1}{\beta n(\lambda)}\right)^2\right\}\frac{d\lambda}{\lambda^2} \tag{3.2}$$

Note that α is the microstructure constant. A water Cherenkov detector is one that uses water as a medium to generate Cherenkov radiation, and SK and HK are examples of this type of detector. As shown in the precedent equation, the intensity of Cherenkov radiation tends to increase with shorter wavelengths. However, considering that the refractive index is not constant with wavelength, in the case of water, Cherenkov radiation is emitted in the region from visible light to near UV light. Since the refractive index of water is $n \simeq 1.33$, when the energy is high enough (when $\beta \sim 1$), $\theta_c \simeq 42°$. As the energy decreases, the Cherenkov angle θ_c decreases and no Cherenkov light is produced when $\beta < 1/n$. The energy threshold for Cherenkov radiation, E_{thr}, is:

$$E_{thr} = mc^2\left(1 - \frac{1}{n^2}\right)^{-\frac{1}{2}} \tag{3.3}$$

From this, the kinetic energy threshold required to generate Cherenkov light can be determined for charged particles. In actual detection, however, the observable energy is larger than this because Cherenkov light cannot be detected without a certain amount of light. PMTs, which can be used to detect Cherenkov light in water Cherenkov detectors, are suitable for this kind of detectors because they have the advantages of a large photosensitive area in addition to excellent single photon detection performance and temporal resolution among optical sensors. Due to the high transmittance of water, the PMT can detect Cherenkov light generated at the center of a tank enlarged by SK.

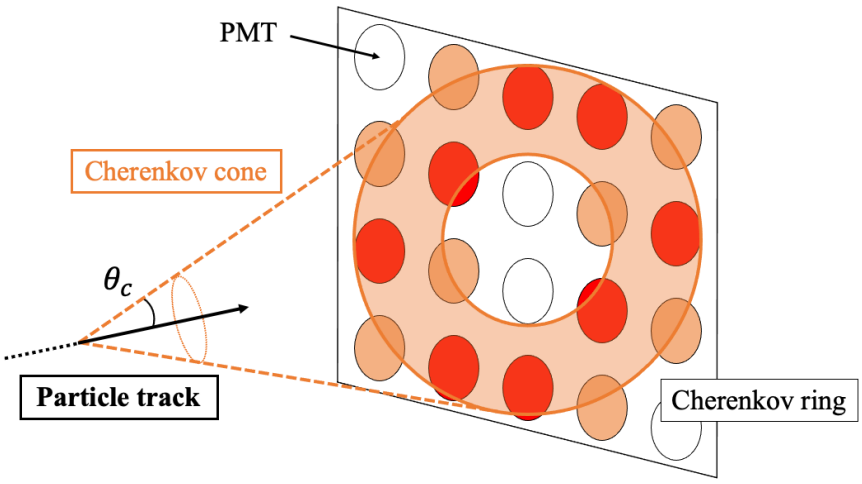

Figure 2.2: Cherenkov light from a charged particle hitting PMT

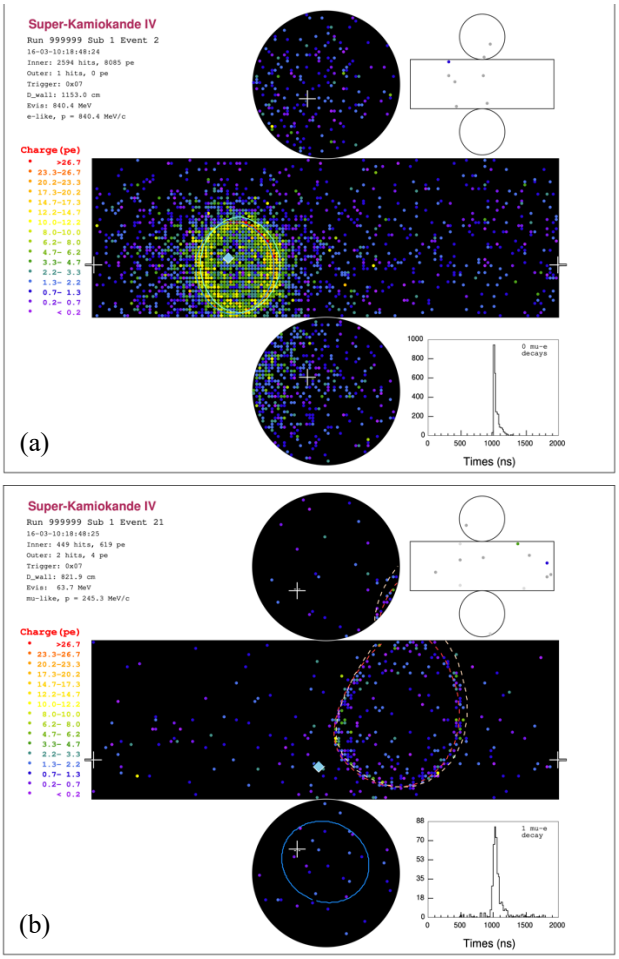

Figure 2.3: Event display of Cherenkov rings created by electrons (a) and muons (b) respectively [16]. The cylindrical detector, where each point represents the position of a PMT and its color represents the number of photoelectrons detected at each PMT.

When electrons and positrons move through water, Cherenkov radiation is generated, and at the same time, gamma rays due to bremsstrahlung are also generated. The process of Compton scattering and electron pair production by the gamma rays is repeated, resulting in the appearance of a shower of unclear rings on the wall surface. In contrast, muons and charged pions are less likely to cause such phenomena due to their large mass, and thus produce a clear Cherenkov ring (Figure 2.3).

PMT

Different types of photomultiplier tubes (PMTs) are used in the inner and outer water layers. The details of these PMTs are described in this section, The details of these PMTs are described in this section. In the inner water layer, 11,146 R3600-5 PMTs manufactured by Hamamatsu Photonics are used. Figure 2.4 shows an overall view. This photomultiplier tube has high transparency in the near-infrared region to about 300 nm, excellent hardness and water resistance, and is virtually unaffected by temperature changes. The photocathode is made of bialkali (Sb-K-Cs), and the sensitive region is from 280 to 660 nm. The quantum efficiency reaches its maximum at a wavelength of about 390 nm, which is approximately 22%. In the outer water layer, 1,857 R1408 photomultiplier tubes manufactured by Hamamatsu Photonics are used. These tubes were used in the IMB experiment. A 60 × 60 cm wave length shifter is installed to increase light collection efficiency and sensitivity. Photons with wavelengths of 300 – 400 nm are absorbed by the shifter and emitted again as photons with longer wavelengths. Some of the secondary photons emitted in this way are reflected in the wave length shifter and enter the photomultiplier tube, where they are detected.

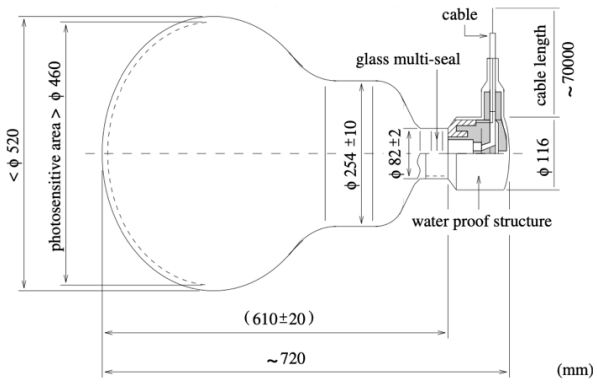

Figure 2.4: 20-inch photomultiplier tube [15]

Chapter 4

Analysis

Simulation

4.1.1 Overview

In this chapter, I will present the core of my internship, which is the simulation of neutrino events in Water Cherenkov detector and their classification. The neutrino interaction classification is extremely important for neutrino oscillation physics since we need to know which neutrinos are interacting. To train our classification model, we need to simulate some events. The simulation tool is the WCSim package from Geant4, and the run has been performed using the Docker installer [17][18]. The data obtained and the classification process will be presented in the following parts. In SK and HK, the event (electron-like, muon-like, and gamma) are classified based on the shape of the Cherenkov ring image, and it's also from these rings that we can reconstruct the vertex positions and directions of the particles produced from neutrino interaction. The event reconstruction process is then crucial for PID.

4.1.2 Software

The sensitivity of SK and HK is determined by the detector structure, the performance of the photosensor, and the photocathode coverage of the entire detector. Therefore, detector simulation is necessary to evaluate the effect of the optical sensor and detector structure on the physical measurement sensitivity. A new detector simulation tool (WCSim) has been developed for Super-Kamiokande and Hyper-Kamiokande, which is a Monte Carlo simulation tool to evaluate the water Cherenkov detector being developed based on Geant4. Geant4 is a widely used simulation package in the field of high-energy physics that can accurately simulate the interaction of particles as they pass through matter [17].

The detector simulation tool "WCSim" is a software for evaluation of water Cherenkov-type detectors that performs Monte Carlo simulations based on Geant4. In Geant4,

physical events are classified into discrete events, events that can be regarded as occurring continuously, and events that occur when the kinetic energy becomes zero. When events are regarded as occurring continuously, they are grouped together and analyzed by interval after dividing the distance into intervals. Ionization loss and Cherenkov radiation are regarded as continuous events. In contrast, events such as electron pair production are evaluated as discrete events. For discrete events, a probability density function is defined with the reaction cross section and the density of the material passing through as coefficients and the length as a variable, according to which the "density length until the next reaction occur" is evaluated and processed accordingly. The following table present the inputs and outputs in the case of the WCSim package [19].

Inputs	Outputs
Choice of the detector geometry (we will input the geometry of SK and HK) PMT Particles to simulate (we will only simulate single particles)	PMT hit charges and times Particle track and PMT information

Table 4.1: Inputs and Outputs for the WCSim package

The Super-Kamiokande geometry has been presented in the previous chapter. On the other hand, we have Hyper-Kamiokande. Hyper-Kamiokande will be a future generation water Cherenkov detector. The design of Hyper-Kamiokande will be contingent on that of Super-Kamiokande, but will engage recently grown PMTs (Hamamatsu R12860). The detector will have better sensitivity to proton decays, meteorological neutrinos, and neutrinos from astrophysical inceptions than Super-Kamiokande (see Appendix A). Hyper-Kamiokande will still be the far detector of a long measure neutrino fluctuation experiment conceived for the improved J-PARC. Hyper-Kamiokande will amount to two tubular tanks, each with dimensions of 60m height and 74m width. The container in Hyper-Kamiokande will have a volume of 258 kilo-tons. The container will exist about 8 km below Super-Kamiokande and 650 m deep under rock. The central detector at Hyper-Kamiokande will hold nearly 45,000 PMTs [20].

To simulate events, I have used the code implemented in the WCSim repository called WCSim.mac. To run events at different energies the code controlling the G4 particle gun has been edited. The default for the particle gun is to run a mono-energetic simulation. Direction and position are defined in the xyz axis from the centre of the tank. To select a different geometry, such as Hyper-Kamiokande, the following edit must be made in the WCSim.mac file. In the following example electrons at 250MeV are generated at the top of Super-Kamiokande (0 0 27 m) and are propagated downwards in the z axis.

```
/mygen/generator gun
/gun/particle e-
#/gun/particle pi0
/gun/energy 5 MeV
/gun/direction 1 0 0
/gun/position 0 0 0

/WCSim/WCgeom SuperK
```

Event display

The data set used in this work consists of single-electron and single-muon events generated with random kinematics and positions in a model of the SK detector. Some simulations have been made without randomity on particle type to test the classification algorithm presented in the following part. The coordinate system used to describe the detector has z pointing along the cylinder axis.

For each simulated event, its particle type, position, direction cosines, and energy, is saved in order to be used during the reconstruction program training. The hit charges and times at every PMT in each event are stored in three two-dimensional arrays representing the unrolled cylindrical barrel of the detector (151×50) and the two circular end-caps (48×48). The data set consists of a hundred files containing each 1000 events (e-like, mu-like and gamma-like). The kinetic energy of the electrons and gamma particle is uniformly distributed between 1 MeV to 1000 MeV and muons between 150 MeV to 1000 MeV. Another set which will be used for the event classification have also been produced and the kinetic energy has been fixed at 250 MeV for the three particles. Spontaneous discharges in the PMTs (noise known as dark rate) has been simulated but will be cleared for simplicity during the classification training. The data obtained after

simulation is in ROOT[3] format. Having had some problems handling these files, and in order to obtain a visualization of the events, they were converted to .npz format. The Figure 3.1 gives a first visualization (2D and 3D). The .npz file extension has one primary file type and is opened with GameGuard(published by INCA Internet). In total, there is one software program associated with this format. In most cases, it is a type of GameGuard Update File format. NPZ files are mainly classified as Data Files and are easily readable with Python using the numpy library.

As mentioned just before, the simulation has been done without omitting spontaneous discharges in the PMT. As we can see in the Figure 3.2, events have a lot of time dispersion which is mainly noise. Here a trimming of the events is done between 900 and 1250 to avoid the noise we mentioned.

[3] ROOT is an object-oriented programming program and software library developed by CERN (https://root.cern)

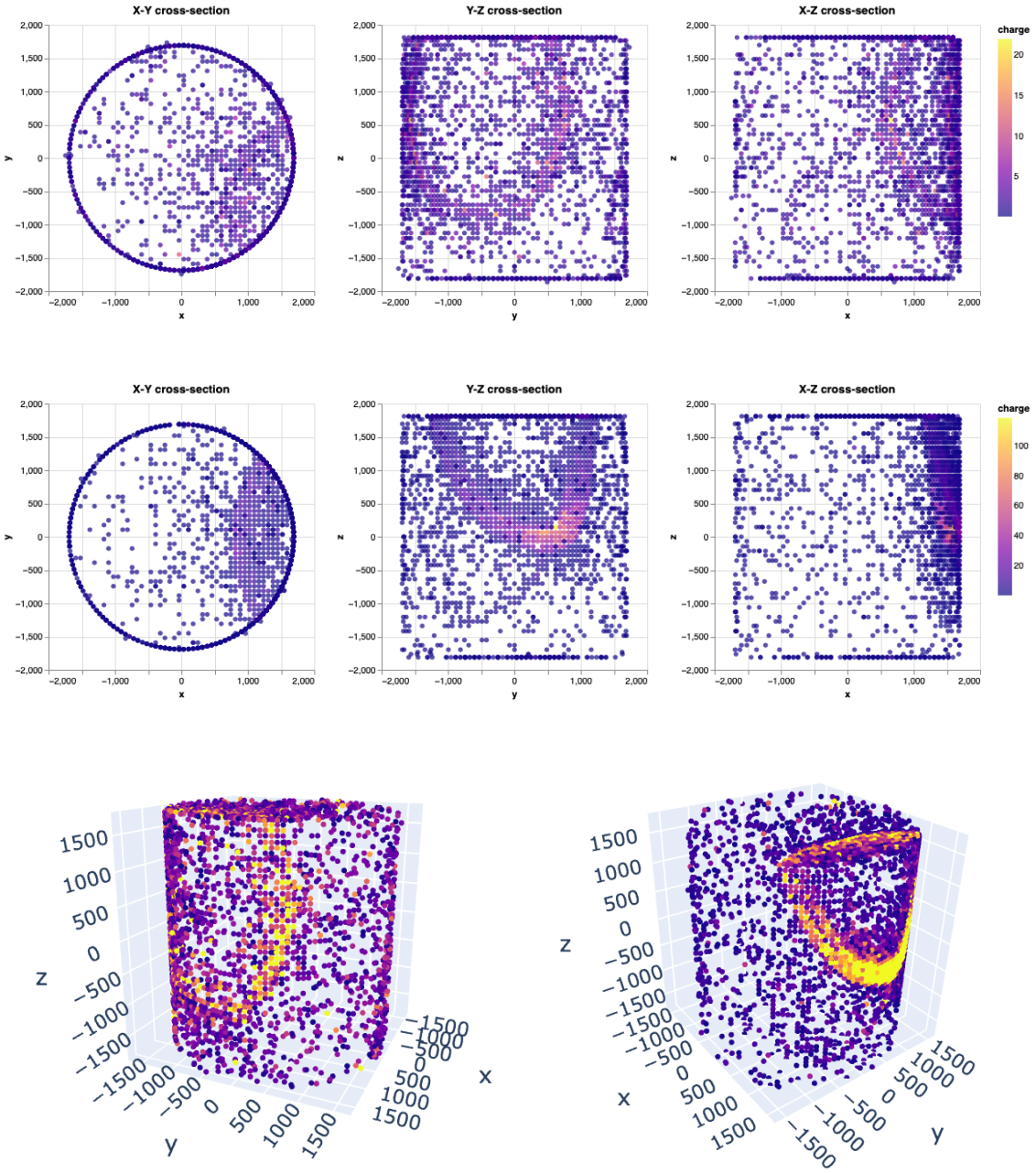

Figure 3.1: WCSim with SK geometry simulated event visualization in 2D and 3D (each point being a hit PMT). The simulation of these events has been done with the knowing particle type input: events from muon-neutrino reactions (bottom and right) and electron-neutrino reactions (up and left) observed in Super-Kamiokande. Charged muons produced by muon neutrinos travel almost straight in water, whereas electrons produced by electron-neutrino reactions create an electromagnetic shower that disturbs the contour of the ring. Charge (in p. e.) is the number of photoelectrons (p. e. stands for photo-electron) and time (ns) is the time (in nanoseconds) it took for the Cherenkov light to reach the photodetector after the event occurred.

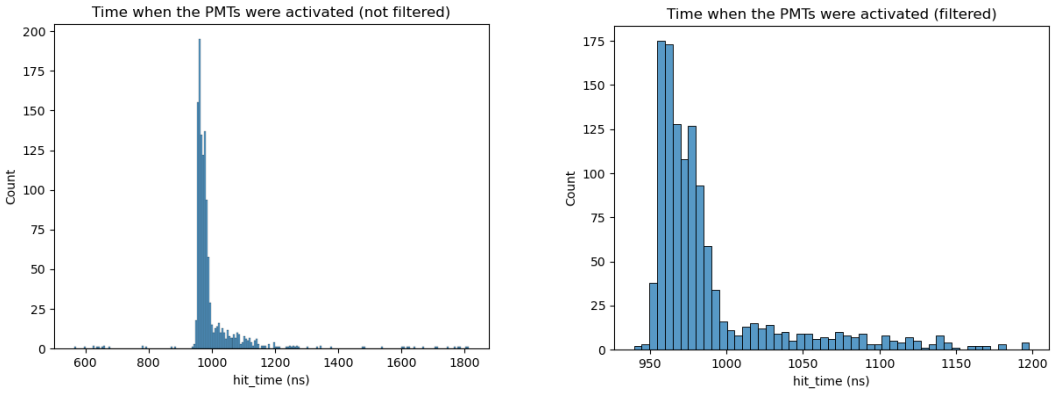

Figure 3.2: PMT hit time in nanoseconds for an electron-like event before and after filtering

Particle Identification

4.3.1 Event reconstruction

Event reconstruction is the process of inferring what events (number of Cherenkov rings, type of particle that generated the Cherenkov light, momentum, etc.) were observed from the information obtained from the detector (time and amount of light observed for each PMT). In this chapter, we describe the event reconstruction algorithm used.

The state-of-the-art in water Cherenkov event reconstruction is the fiTQun maximum likelihood estimation algorithm [21]. FiTQun is a modified version of the algorithm developed for the MiniBooNE experiment for the T2K experiment. It uses the maximum likelihood method based on the charge and time information observed at each PMT to reconstruct information such as the type, generation point, direction, and momentum of the particle that generated the Cherenkov ring.

The reconstruction is performed using the following likelihood function:

$$L(x) = \prod_{j}^{unhit} P_j(unhit|x) \prod_{i}^{unhit} (1 - P_i(unhit|x)) f_q(q_i|x) f_t(t_i|x) \qquad (4.1)$$

where x is a function including the coordinates (x, y, z) of the point of origin, time t, zenith angle θ, azimuth angle φ, and momentum p. $P_j(unhit|x)$, $(1 - P_i(unhit|x)$ denote the probability that the PMT will not and will hit, respectively. Also, $f_q(q_i|x)$ and

$f_t(t_i|x)$ are probability density functions of observed momentum and time, respectively. The momentum and time probability density functions are generated based on the detector responses to a large number of electron, muon, and pion events simulated by changing the momentum, position, and direction of generation in the detector.

In fiTQun, the event reconstruction is performed by changing the parameters so that the likelihood function is maximized, i.e., $-\ln L$ is minimized.

However, this process leads to certain problems. Mo Jia et al. explain very well the current situation [25]. "*In order to make this likelihood function tractable, it is factorized into several low-dimension components. In particular, the PDFs associated to Cherenkov photons that produce a hit without having scattered in the water or reflected in the detector surfaces are factorized from the PDFs that describe so-called indirect photons that scatter or reflect before producing a PMT hit. The level of detail of the indirect photon PDF is limited by the high number of dimensions required for it to be fully specified. In particular, this limitation makes it difficult to reconstruct heavier, typically slower, particles such as protons, since it is challenging to accommodate the effect of the decreasing Cherenkov photon emission angle. Finally, each component of the factorized likelihood needs to be tuned separately to the detector geometry of interest, requiring a large amount of bespoke simulated data with different components of the simulation disabled in turn*." The problem faced was then the running time for the reconstruction.

4.3.2 Convolutional Neural Network

To overcome this challenge, the solution I chose was to replace this likelihood function by a simple Convolutional Neural Network for binary classification. As we have seen in Figure 2.3 and 3.1, the shape of the Cherenkov ring is one way to classify events and the use of CNN is then relevant. A CNN (or Convolutional Neural Network) is an artificial neural network with at least one convolution layer. A convolution layer is a layer in which a certain number of convolution filters are applied. But why apply convolution filters? Simply because an image contains lots and lots of input data. Indeed, we have to find an approach other than the classic ANN (or Multilayer Perceptron) networks. The idea behind convolution filters is that they can be used to find patterns or shapes in images. In effect, CNNs enable to gradually determine the various shapes and then assemble them to find others.

The architecture of such a network is very often based on a stack of convolutional layers, followed by deep, dense layers that do the decision-making (see Appendix B). To sum up, the convolution layers find the shapes and patterns in the image, and the final layers perform the decision-making work (such as classification, for example).

Convolution layers comprise several filters. Each convolution filter – as we explained earlier – on the same layer will therefore extract or detect a feature from the image. Thus, at the output of a convolution layer we have a set of features that are materialized by what we call Feature Maps (see Figure 3.3).

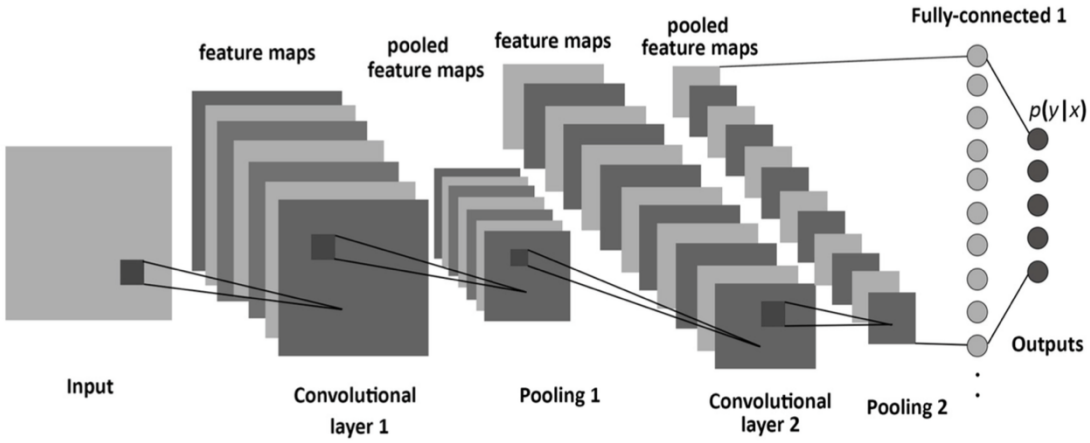

Figure 3.2: Classic architecture of a convolutional neural network [23]

The model creation is explained in the Appendix B. However, the CNN is used to classify images. It is then necessary to convert the simulated data into images. In order to generate an image where each PMT is represented as a pixel, it is necessary to map each coordinate in PMT space to a pixel in the plane. For that, we will produce a geometry file mapping all the PMT in Super-Kamiokande and Hyper-Kamiokande. After the conversion, the resulting array has the form (number of event, 151, 50, 2), i.e., the number of images is the number of simulated events, and each image is 151×50 with two channels: charge received by PMT and time when it was activated. The images obtained are as followed.

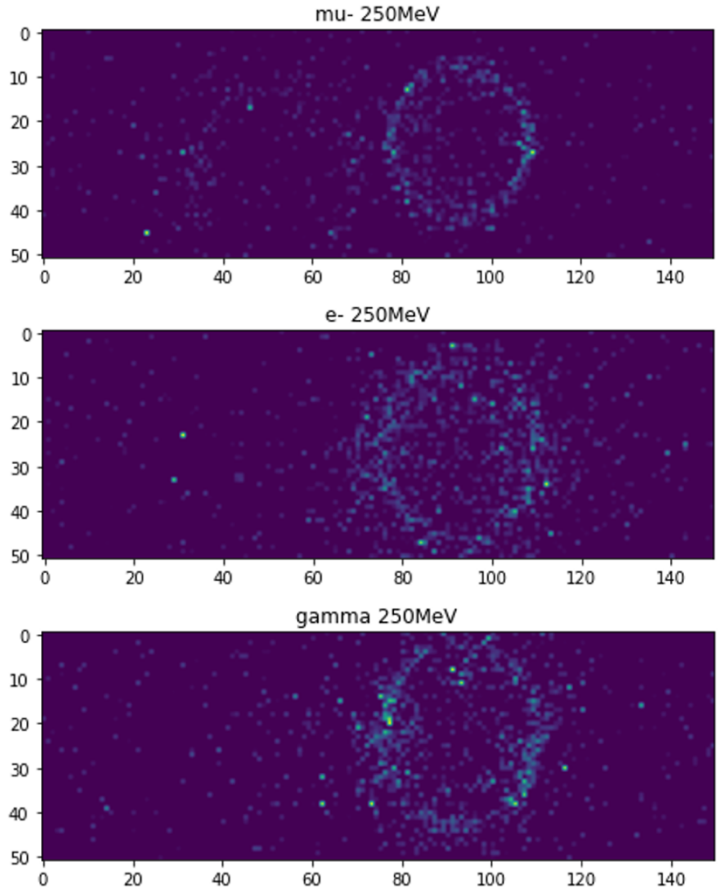

Figure 3.3: Converted images for a 1000 events (electron, muon, gamma) with an energy of 250 MeV, direction: 1,0,0 (non-filtered). The particle is known to have an idea of the ring shape. As the event is known, those data will be used for the classification training.

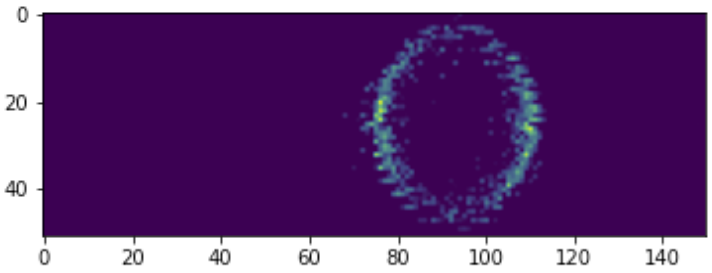

Figure 3.3: Converted images for a 1000 event with an energy of 250 MeV (filtered). Some noise remains and could have an impact on the classification model training.

4.3.3 Performance Analysis

For the training of the classification model, the data have been separated as follows: 70% training and 30% testing. The results of the classification are shown in Table 4.2 and Figure 3.4 and 3.5. First, we have a look at the results for the Super-Kamiokande simulation. I have first make a training of my model by dividing my sample as follows: Train 70%, Test 30%. To get a better understanding of Table 4.3 Figure 3.4, we remind:

- accuracy: amount of correct classifications over the total amount of classifications.
- train accuracy: accuracy of the model on the 70% of the sample it was constructed on.
- test accuracy: accuracy of a model on the 30% it hasn't seen.

In Figure 3.5, he ROC (Receiver Operating Characteristic) curve represents sensitivity (true positive rate) as a function of 1 − specificity (false positive rate) for all possible threshold values of the marker studied. Sensitivity is the test's ability to detect electrons, and specificity is the test's ability to detect muons or gamma. The area under the ROC curve (or Area Under the Curve, AUC) can be interpreted as the probability that, out of two randomly chosen events, the marker value is higher for the electron. Thus, an AUC of 0.5 (50%) indicates that the marker is non-informative. An increase in AUC indicates an improvement in discriminatory abilities, with a maximum of 1.0 (100%).

The accuracy for e-like and mu-like events classification is very high (99%). Moreover, the AUC is at 1.00 and indicates the highest degree of separability between the two events. Higher precision with a higher number of events is however needed to get a more precise value of the AUC. Indeed, by looking at the Figure 3.4, we observe a good differentiation between electron-like and muon-like events but still some unidentified regions. This can be due to other noises since the filtering has been done after the simulation. The accuracy of the e-like and gamma-like events classification is less as we expected by looking at the Cherenkov rings, but is still decent regarding the fact that the classification has been performed image-based only.

The classification model training has also been performed on Hyper-Kamiokande simulation. For now, it has only been performed for the e^-/μ classification and with 100,000 events each (500 MeV) to also test the running time of the CNN classification. As expected, the accuracy dropped by 10% in comparison with the training made with the Super-Kamiokande simulation. It is still a good accuracy, and the PID likelihood

distribution (Figure 3.6) indicates that the e-like and μ-like events are well separated, the probability of misidentification being about 11%. Regarding the computational time, I obtained a training time of 10,000 events in 1 minute. This result should be compared to the classification time for the fiTQun algorithm (see next part).

	Super-Kamiokande		**Hyper-Kamiokande**	
	Accuracy (%)	*AUC*	*Accuracy (%)*	*AUC*
e^-/μ	99 ± 0.1	1.00	99 ± 0.02	0.892
e^-/γ	67 ± 0.11	0.696	–	–

Table 4.2: Accuracy and AUC (Area Under the ROC Curve) of the classification by simple CNN for binary classification. Performed with a sample of 1000 events each with kinematic energy of 250 MeV.

As we can observe on Figure 3.4 and 3.5, the model undergoes some overfitting in the case of classification of electron-like and gamma-like event. The model adapts too well to the training data, to the point of losing generality, and therefore not working well with new data. Over-fitting occurs in particular when the model is too complex for the amount of data available. This problem has occurred in the algorithm and the addition of dropout layers (see Appendix B) has fixed it for the electron/muon classification but remains a challenge for the electron/gamma one. With more time, I should be able to fix it. We can however take a look at the ROC curve. The AUC obtained (0.696) indicates a good prediction from my CNN model. Some comparison will be made in the next part.

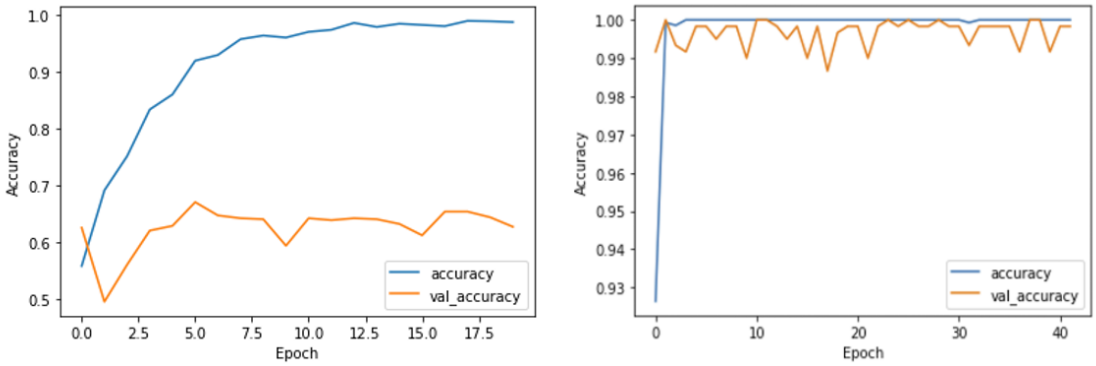

Figure 3.4: Test (val_accuracy) and train (accuracy) accuracy of the simple CNN for binary classification model for the electron-like/gamma-like identification (left) and electron-like/muon-like classification

(right) with the Super-Kamiokande simulated data. One epoch corresponds one complete pass of the training sample through the model.

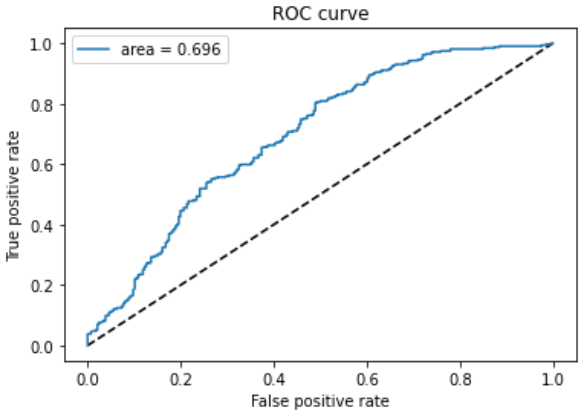

Figure 3.5: ROC curve and AUC for the simple CNN for binary classification model testing for electron-like/gamma-like identification with the Super-Kamiokande simulated data

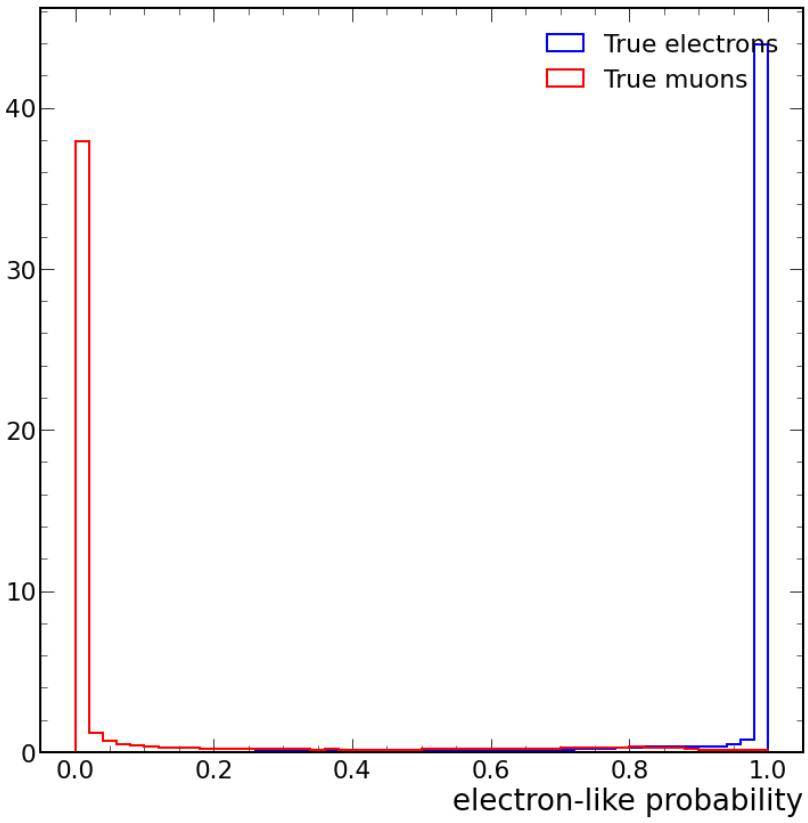

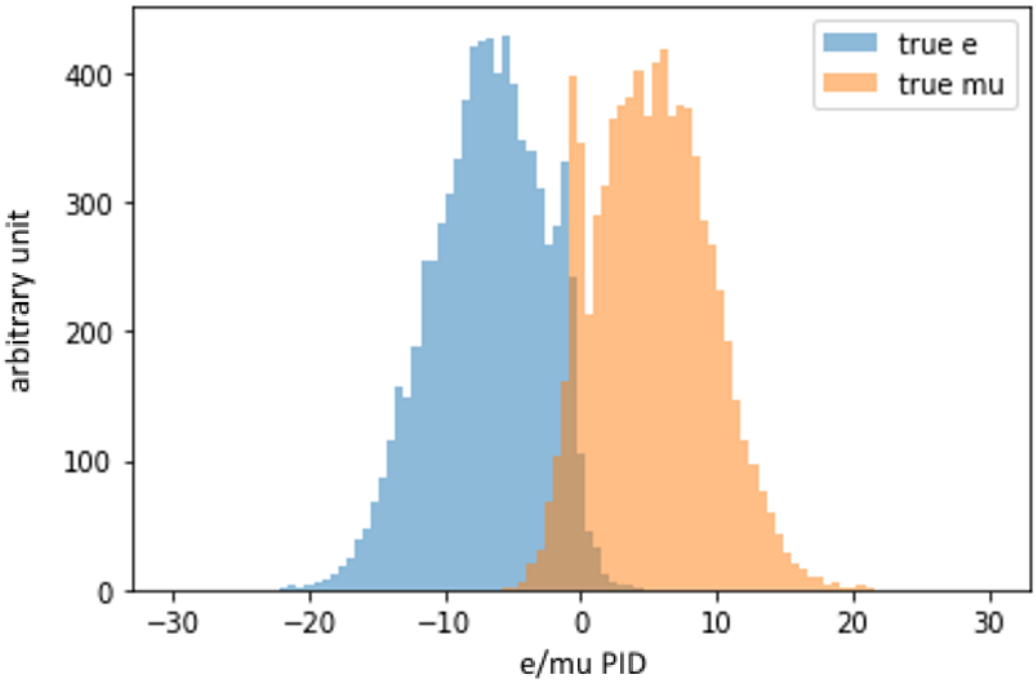

Figure 3.6: Electron-like probability for simulated SK atmospheric neutrino events (up). Log-likelihood distribution for simulated HK atmospheric neutrino events (bottom). Note that for HK, we only take into account events with an allowed vertex distance to the wall > 100cm.

4.3.4 Comparison with Data

The CNN model has been developed using simulated events of electrons and muons with well-known energy and momentum. The crucial test for this model is its performance on real data.

First, let's take a look at the performance comparison between the reconstruction/ classification method. For the comparison regarding the reconstruction time, I will base my analysis on the paper from M. Jiang et al. [21] and Mo Jia et al. [22]. Regarding the running time, the fiTQun algorithm runs 1 event in 1 minute [21]. On the other hand, after being trained, the Generative Neural Network model developed by Mo Jia et al. has a reconstruction time of 100,000 events in 1 minute, which is better than the CNN model developed during this internship. On the basis of more than 1,000,000 simulated events, Mo Jia et al. are exploring an alternative use of CNNs in water Cherenkov reconstruction by generating PDFs at each PMT for maximum-likelihood estimation. The computed loss function has been designed in a similar way to the one of the fiTQun algorithm but only describe the probability of the PMT being hit and the probability density function for a

hit charge and time, which explain the faster reconstruction time. In order to accommodate the unknown functional form of the hit charge and time PDF, Mo Jia et al. approximate this function with a weighted mixture of Gaussian PDFs in one or two dimensions (hit charge and time). Initial studies are encouraging and demonstrate that smooth and unbiased likelihoods can be achieved (Figure 3.7).

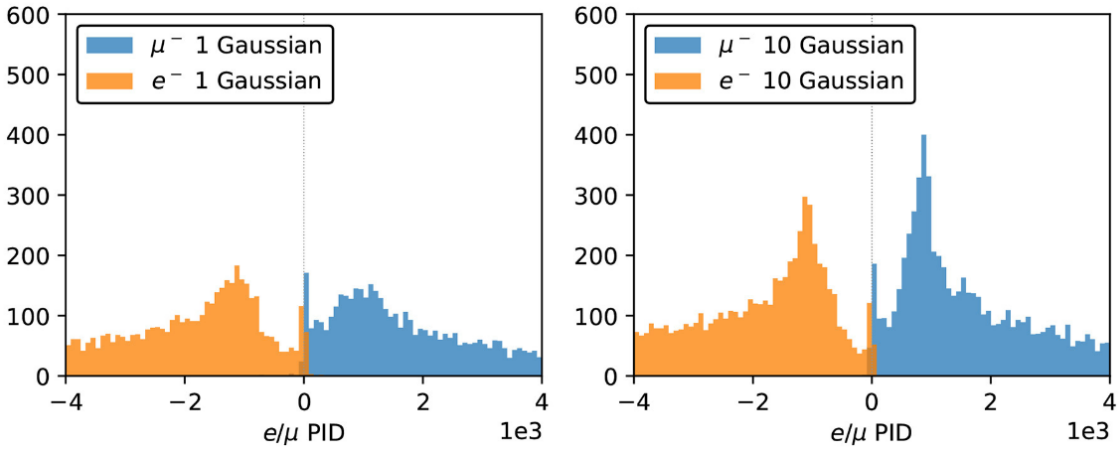

Figure 3.7: PID performance of the 1-Gaussian (left) and 10-Gaussian (right) charge-only networks. The true electron and muon events are located in the negative and positive regions, respectively, and the 10-Gaussian network shows better concentrated peaks for both particle types. As we can see, the probability of misidentifying is very low, especially for a very high number of simulated events.

As mentioned, the real test for my CNN model is its application on real data. To make this comparison, I have used data from the Water Cherenkov Machine Learning repository on GitHub [24]. The results are shown in Figure 3.8. The data was reduced to a thousand events to compare the probability of particle type with the simulated date. As we can observe, the electron-like and muon-like events are well separated (the noise has not been cleared), and the electron-like and gamma-like events are also well-separated, the misidentification rate being only 40% (giving an accuracy close to the one obtained during the CNN model training with simulated events).

Some comparisons have also been made for the case of electron/gamma classification. As mentioned earlier, the overfitting issue of my model is not fixed. It is, however, possible to compare the classification performance with regards to the efficiency of the CNN, with other classification methods results. For this, I have taken as a comparison the MVA (Mean Value Analysis) Classification Methods for simulated Super-Kamiokande events, described by Baran Bodur and Kate Scholberg [26]. The inputs of the simulation done by Baran Bodur and Kate Scholberg are as follows: single-ring events, electron-like and no

decay of electron, energy below 100 MeV. The output of the MVA provides visible separation between “electron” and “electron and gamma” events (Figure 3.9). The plotted ROC curve can be put in comparison with Figure 3.5. In Baran Bodur and Kate Scholberg’s model, when separating events with $E > 3$ MeV gamma rays, 62% background rejection at 80 % efficiency is achieved. In comparison, only 51% is achieved at the same efficiency. Our model’s performance are however good, taking into account the energy difference of the two samples. As Baran Bodur and Kate Scholberg mentioned, better performance at lower energies are achieved due to lower scattered hits. Indeed, the background rejection drops below 60% at 80% efficiency for 110-120 MeV events. It is then safe to say that my CNN model performance are consistent with other classification method’s performance.

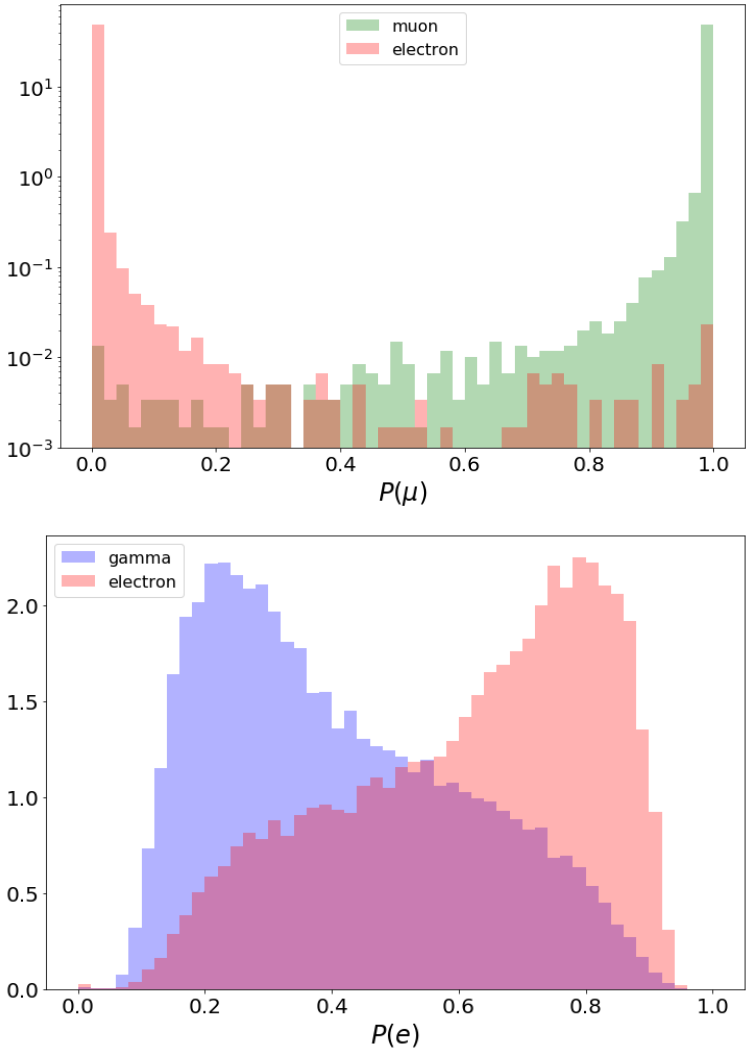

Figure 3.8: : Result of my CNN model for muon-like probability for real SK atmospheric neutrino event (up) and electron-like probability for real SK atmospheric neutrino event (bottom).

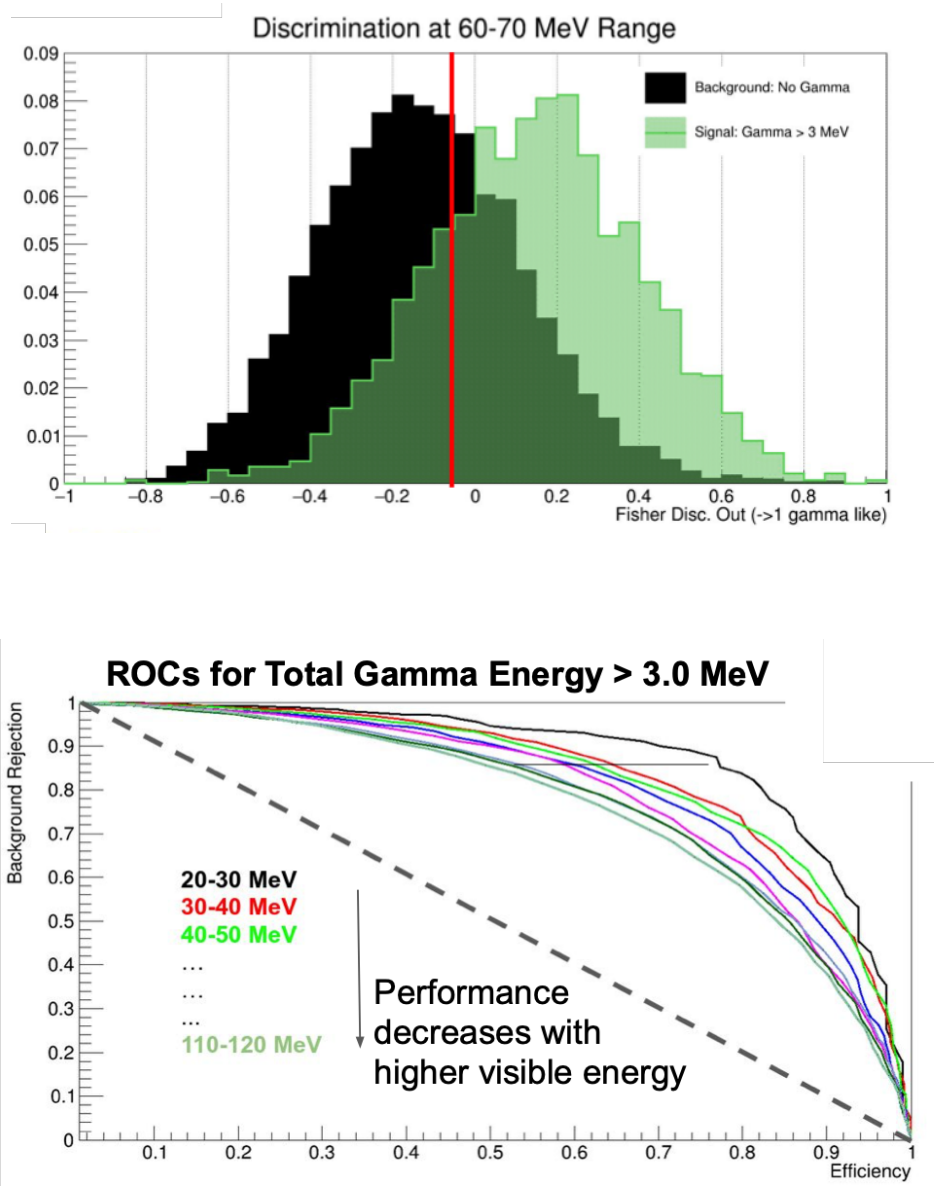

Figure 3.9: Baran Bodur and Kate Scholberg gamma-like probability for simulated SK atmospheric neutrino event (up) and ROC curve for the performance of the MVA classification method for gamma tagging across energies from 20 – 120 MeV (bottom) [26].

Chapter 5

Conclusion

During this internship, I was able to simulate and display various neutrino events detected by Water Cherenkov detector pretty well. An algorithm for particle identification of atmospheric neutrinos with Water Cherenkov detector has been developed. This machine learning algorithm is based on CNN for binary image classification and has only been computed to classify particle type events in two classes. Therefore, some modifications need to be made in the case of multiclass classification.

However, good results have been produced. The simulations and their display are satisfying, even if some issues regarding the display with ROOT forced me to change the simulated data format. This was, however, necessary to transform the data into images to perform the CNN model training and the classification. The accuracy of the model was very high and its performance in the identification of electron-like and gamma-like events was unexpectedly good $\left((67 \pm 0.11)\%\right)$ accuracy. Moreover, its application to real data and its short running time (10,000 events in 1 minute) make this model very interesting for low numbers of events.

Of course, this work is preliminary in many ways: the model training was made with a filtered sample ; the simulation of a very large number of events with very high energy has not been performed yet, ...

The various works carried out during this internship, however, made it possible to highlight the importance of the classification of neutrino events in the understanding and future analysis of neutrino physics with Water Cherenkov detector. This internship was a fantastic experience and taught me a lot, both in terms of knowledge in particle physics, and in the research work in a scientific laboratory. This internship was also an opportunity to validate my choice of professional orientation towards particle astrophysics. From a more general point of view, this experience taught me a lot and made me want to pursue this orientation abroad in order to discover not only new workplace but also new scientific knowledge.

Appendix A

Hyper-Kamiokande physics

This chapter summarizes the physics covered by HK.

A.1 Atmospheric neutrino

A.1.1 Overview

Primary cosmic rays such as protons and helium nuclei interact with nuclei in the atmosphere above to produce hadron showers of pions and K mesons. These mesons decay in flight to produce neutrinos, called atmospheric neutrinos. The main production processes are:

$$\pi^+ \rightarrow \mu^+ + \nu_\mu \quad \text{(A. 1.1)}$$

$$\mu^+ \rightarrow e^+ + \nu_e + \overline{\nu_\mu} \quad \text{(A. 1.2)}$$

The primary cosmic ray flux is nearly isotropic with respect to the Earth, and the resulting atmospheric neutrino flux will be present at all zenith angles. Atmospheric neutrinos have no control over where and when they are generated, but their energies are widely distributed, from about 100 MeV to over 1 TeV, and their flight distances can range from 10 km to 10,000 km. Therefore, new physics can be explored in a wide range of parameter domains. Atmospheric neutrino observations have also led to the discovery of the $\nu_\mu \rightarrow \nu_\tau$ oscillation.

At HK, more detailed measurements of intergenerational neutrino oscillation probabilities will be made using high-statistics data. However, atmospheric neutrinos are a serious background for proton decay searches. The identification of neutrino events, discussed in Chapter 4, is used as one of the methods to remove the background and to discriminate between neutrino and antineutrino events. One of the main goals of atmospheric neutrino observations is to determine the mass ordering.

A.1.2 Neutrino mass ordering

With the discovery of neutrino oscillations, neutrinos are known to have masses, and their squared differences have been measured. However, the order of the masses of the three types of neutrinos has not yet been clarified (the mass ordering problem). The case $m_1 < m_2 \ll m_3$ is called the normal ordering, and the case $m_3 \ll m_1 < m_2$ is called the inverted ordering (Figure A.1). From a theoretical point of view, the mass ordering is important as a clue to understand neutrino mass mixing, and may also influence the observation of $0\nu\beta\beta$ decays when the neutrino is a Majorana particle. However, as shown in Eq. 1.3.8 for oscillations between two generations of neutrinos, it does not depend on the sign of Δm^2, making the sign determination difficult. A promising method for determining the mass ordering is to use the matter effect (MSW effect): as discussed in section 2.2.1, neutrinos can interact with matter in flight, but the electrons present in the matter cause reactions that only electron neutrinos undergo. The effect of the amplification or suppression of the oscillation probability of $\nu_\mu \leftrightarrow \nu_e$ due to the difference in interaction between the three types of neutrinos is called the matter effect. The effect on the oscillation probability depends on the neutrino energy, the flight distance, and the density of the matter passing through, and also depends on the mass ordering.

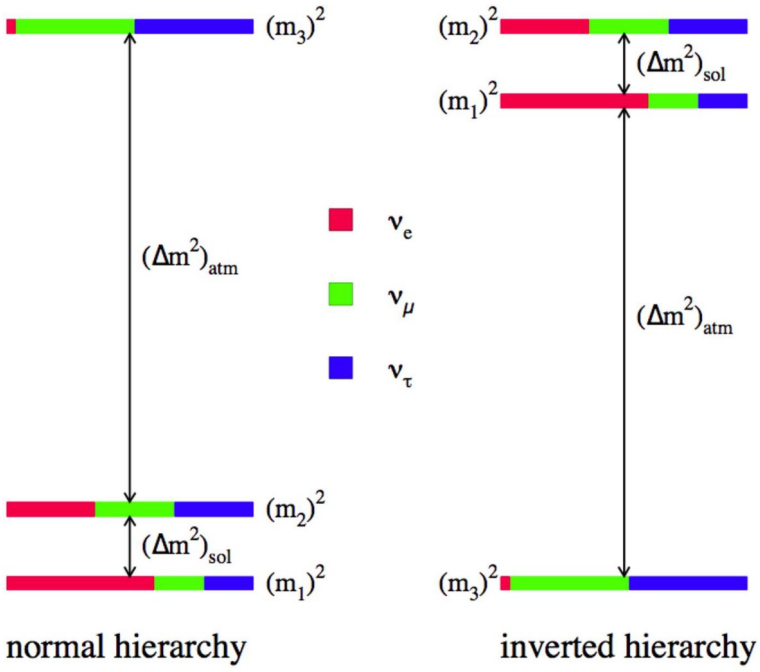

Figure A.1: Definition of mass ordering [22]

HK aims to determine the mass ordering from material effects of atmospheric neutrinos, especially when they pass through the Earth's interior. Assuming a forward ordering, when neutrinos with energies of 2-10 GeV pass near the center of the earth, the oscillation probability is greatly amplified by resonance, and the effect is different for neutrinos and antineutrinos depending on the mass ordering.

The advantage of HK is that it can improve the accuracy of its measurements by combining data from atmospheric neutrinos and accelerator neutrinos, which are sensitive to multiple oscillation parameters, including mass ordering. Figure A.5 shows the expected measurement sensitivity for mass ordering determination from the combined analysis of accelerator and atmospheric neutrinos. Although the sensitivity depends on the value of θ_{23}, it is better than $\sim 3\sigma$ at rejecting false mass orderings when the forward or inverse ordering is correct after 5 years of observation, and even in the least sensitive region, the mass ordering can be determined at 3.8σ after 10 years of observation.

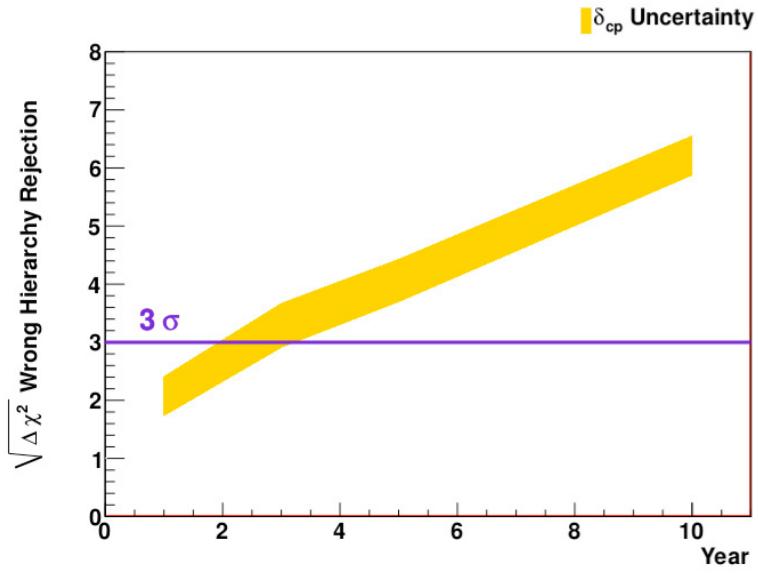

Figure A.2: Change over time in sensitivity of measurement of mass ordering expected from combined analysis of HK accelerator neutrinos and atmospheric neutrinos [30]

Other neutrino oscillation parameters can also be measured with much higher accuracy than previous studies. HK can determine the θ_{23} octant over a wide range of parameters. 10 years of atmospheric neutrino data alone can determine the θ_{23} octant at 3.8σ when $|\theta_{23} - 45| > 4°$, the octant can be resolved at 3σ, and when combined with the results of accelerator neutrino observations, the octant is expected to be resolved up to 2.3σ. In addition, for event identification, tau-neutrino appearance events due to $\nu_\mu \rightarrow \nu_\tau$

oscillations can be measured by a statistical method using a trained neural network. A significant tau-neutrino signal has already been observed in SK, and a more positive signal in HK is expected. The HK is expected to measure the probability of oscillation to tau neutrino and the reaction cross-section more precisely.

A.2 Solar neutrino

Solar neutrinos are electron neutrinos produced by thermonuclear fusion reactions near the center of the Sun, and there are two types of reactions: pp-chain and CNO-cycle. CNO-cycle is dominant at central stellar temperatures $\geq 1.6 \times 10^7$ K, but its contribution to the Sun with a central temperature of $\sim 1.6 \times 10^7$ K is only about 1.6%. Therefore, the main reaction pathway is pp-chain ($4\mathrm{p} \rightarrow \mathrm{He} + 2\mathrm{e}^+ + 2\nu_\mathrm{e}$).

Since neutrinos hardly interact with matter and are emitted from the Sun much faster than light, real-time solar neutrino observations enable us to monitor the current state of the solar center. In addition, since solar neutrinos pass through dense matter in the solar interior to reach the Earth, they are also affected by matter effects, making it possible to study neutrino propagation in matter. In the case of HK, solar neutrinos are detected through the atmosphere during the daytime, whereas they are detected through the Earth's interior during the nighttime. Therefore, when solar neutrinos propagate through the Earth's interior, the matter effect in the Earth's interior causes some of the muon-tau neutrinos, whose flavor is changed by the matter effect in the Sun, to revert to electron neutrinos.

The solar neutrino energy spectrum has been predicted by the Standard Solar Model [28], and in the 1990s, large detectors such as SK and SNO have made high-precision solar neutrino observations possible. The solar neutrino measurements are made by combining the solar neutrino observations with the reactor antineutrino data from the KamLAND experiment. While the mixing angle θ_{12} is consistent between solar neutrinos and reactor antineutrinos, there is a difference of about 2σ in Δm^2_{12}. The accuracy of the measurement of the day-night asymmetry in the observed fluxes has been improved in HK, and the truth of this difference can be verified with an accuracy better than 4σ. If the Δm^2_{12} difference between solar neutrinos and reactor neutrinos is accepted, new physics will need to be introduced.

A.3 Supernova neutrino

Neutrino observations provide information about the interior of astronomical objects that cannot be obtained by optical observations. Neutrinos produced by core-collapse supernova explosions, which are the final stage in the evolution of stars more than eight times more massive than the Sun, are a typical example, and their observations can provide information on the conditions inside supernovae and the time evolution of the explosions.

A.3.1 Supernova

At the final stage of their evolution, stars undergo a phenomenon called a supernova explosion. Supernova explosions are classified into Type I and Type II according to optical observations. In order to observe supernova explosions by neutrino observations, HK is focusing on gravitational collapse supernova explosions with neutrino emission. A Type II gravitational collapse supernova explosion, in which a star more than eight times the mass of the Sun collapses due to its own gravity, releases enormous gravitational energy (10^{53} erg), 99% of which is emitted as neutrinos. In this section, we describe the neutrino generation process in a gravitational collapse supernova explosion (Figure A.3).

A massive star, which is more than eight times heavier than the Sun, goes through red-giant and red-supergiant stages before finally exploding as a supernova. After the birth of a star, nuclear fusion of light nuclei such as hydrogen and helium produces heat and light, which in turn produces heavier nuclei, and finally iron is produced by the nuclear fusion of silicon. When the center of a star is formed by iron, energy cannot be released by fusion to heavier elements anymore, and the balance between the pressure gradient and gravity that supported the star is lost, and the star collapses. At this time, iron, which forms the central core of the star, collapses gravitationally into a mass of neutrons, generating an enormous amount of energy. This energy is the source of the gravitational collapse supernova explosion, as well as the source of a large amount of neutrino emission. The energy released reaches about 3×10^{53} erg, leaving behind a stellar core that becomes a neutron star or black hole and a supernova remnant. In the process, elements heavier than iron, such as zinc, gold, and silver, are synthesized and ejected (supernova elemental synthesis). Supernova explosions are extremely rare, occurring only once every few decades in a galaxy.

A typical supernova neutrino ejection begins when the nucleus is split into protons and neutrons, and the protons release 10^{51} erg of energy in about 10 ms via a neutron burst ($p + e^- \rightarrow n + \nu_e$). The gravitational energy is then converted to thermal energy, and energy is extracted by the production of a whole generation of neutrinos and antineutrinos during the next 100 ms to 1 s. The energy of the neutrinos is then converted to thermal energy and energy is extracted by the production of antineutrinos during the next 100 ms to 1 s. Thus, 99% of the energy of a supernova explosion is emitted as neutrinos. These neutrinos have an energy spectrum that corresponds to the temperature inside the supernova, and they have information on the time evolution of the explosion.

On February 23, 1987, Kamiokande, IMB, and Baksan were the first to observe neutrinos from SN 1987A.

The number of events observed was the highest in the world. Although the number of observed events was only 24 in all, the theory of supernova explosions due to gravitational collapse was proven to be basically correct. However, the detailed mechanism of the explosion has not yet been clarified. The models that have succeeded in simulating supernova explosions depend on the shape of the supernova neutrino flux and energy rise time, and if the HK experiment, with its larger and more accurate detector, can provide observational data on supernova neutrinos, the prediction accuracy of each model will be improved. The prediction accuracy of each model will be improved if we can obtain observational data of supernova neutrinos from the HK experiment, which has a larger and more precise detector than SK.

A.3.1 Supernova Relic Neutrino (SRN)

Supernova background neutrinos (SRNs) are neutrinos produced by supernova explosions between the birth of the universe and the present. SRNs fill the present universe, and their flux is estimated to be tens of cm/s (Figure A.4). The expected inverse β reaction in SK is 0.8 $\sim$ 5 events/year above 10 MeV, but no SRN signal has been observed due to the background of spallation products and low-energy atmospheric neutrinos. SK-Gd is currently underway to reduce the background, lower the energy threshold, and tag neutron events to identify true inverse beta reactions and detect the SRN signal in SK. Assuming a typical theoretical model, SK-Gd is expected to observe a 4σ signal in 10 years, and further observations at HK are expected to provide insight into the temperature inside supernovae, star formation frequency, black hole formation, ...

The observations at HK are expected to provide a better understanding of the temperature inside supernovae, the frequency of star formation, black hole formation, ...

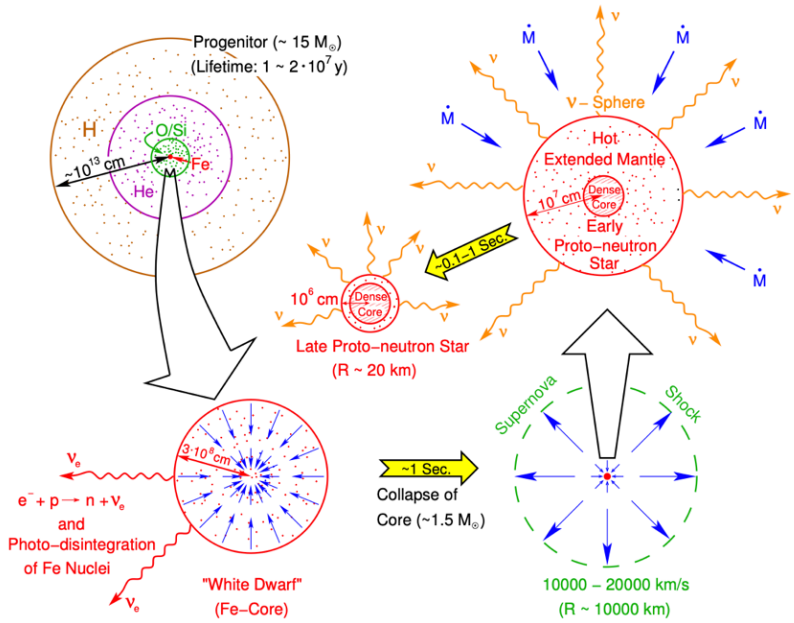

Figure A.3: Overview of the time evolution of a gravitational collapse supernova explosion [28].

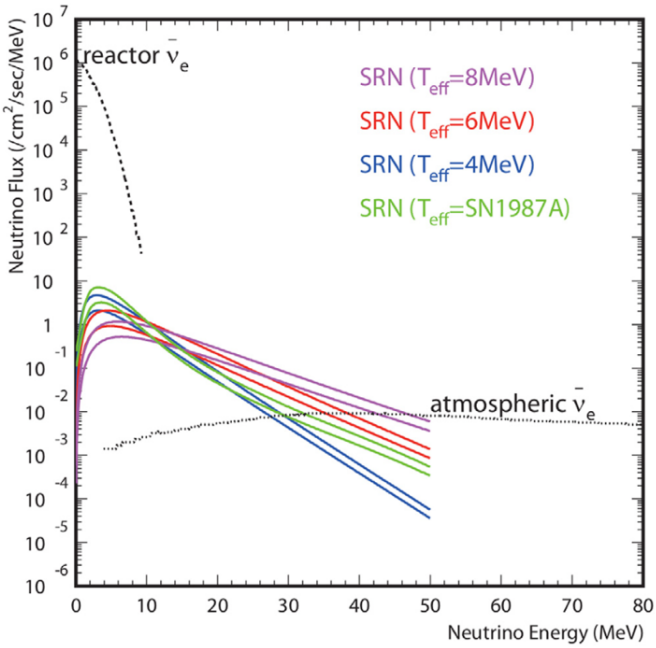

Figure A.4: Predicted supernova background neutrino (SRN) spectra. Fluxes of reactor neutrinos and atmospheric neutrinos are also shown [27].

A.4 Proton decay search

In addition to CP symmetry breaking, baryon number breaking is also necessary to explain the matter-antimatter asymmetry in the present universe. Sakharov proposed proton decay as a baryon number breaking process, citing the necessary conditions for the evolution of the early universe, where particles and antiparticles are thought to have existed in equal numbers, but this phenomenon has not yet been observed. To significantly increase sensitivity from SK, HK requires a large number of nucleons to be observed and sufficient reconstructive power to detect and suppress background signal events.

A.4.1 Grand Unified Theory (GUT)

It is considered to be part of a more comprehensive theory because the standard theory of elementary particles cannot account for the fact that the baryon number is conserved and that the magnitudes of the charges of protons and electrons coincide with high precision (the problem of quantization of charge). The GUT integrates quarks and leptons in a structure with larger symmetries, including the gauge group of the standard theory. By treating them in a unified manner, it predicts baryon number breaking and gives a natural answer to the problem of charge quantization. It has also been suggested that the coupling constants of the electromagnetic, weak, and strong forces converge at energies as high as 10^{16} GeV, which is why the GUT is considered a strong candidate. However, the current accelerator energies are on the TeV (10^3 GeV) scale, making observation difficult. On the other hand, GUT predicts nucleon (proton or bound neutron) decay, albeit very long-lived, and direct verification of GUT is possible if proton decay can be observed. GUTs based on different gauge symmetries (e.g., SU(5) and SO(10)), the leading one predicts a proton lifetime of $\tau_p \sim 10^{35}$ years. The current lower limit on proton lifetimes is about an order of magnitude shorter, although the allowed theory and interactions have been limited so far mainly by observations at SK. HK is a giant detector containing 6 × 1034 protons (5 × 1034 neutrons) in its effective volume and has proton decay detection sensitivity for many models of GUT.

A.4.1 Mode of nucleon decay

Various modes of nucleon decay are predicted by each model of the GUT. One of the most promising proton decay modes is:

$$p \rightarrow e^+ + \pi^0 \qquad (A.4.1)$$

The π^0 immediately decays into two photons, forming an electromagnetic shower in the water as well as e^+, and all the particles in the final state become observable, so the proton mass can be reconstructed. The two photons produced by the decay of π^0 may be close enough in space to be reconstructed as a single ring, so events with two or three Cherenkov rings originating from electrons or γ-rays are selected. In addition to cutting the reconstructed energy, the background such as atmospheric neutrino-derived events with neutrons in the final state is removed by requiring no neutron events in the final state by neutron identification to improve sensitivity. The background is verified by measurements from the K2K experiment, where the background of atmospheric neutrinos for $p \rightarrow e^+ + \pi^0$ searches without neutron identification is expected to be $1.63\ ^{+0.42}_{-0.33}(stat) + ^{+0.44}_{-0.51}(sys)$ events/(1 Megaton year) [31].

The GUT, assuming supersymmetry, predicts decay modes such as:

$$p \rightarrow \bar{\nu} + K^+ \qquad (A.4.2)$$

In this case, no final-state neutrinos are observed, and the K^+ produced by the decay also has a momentum below the threshold of Cherenkov emission (Table 2.1). Therefore, the search for this decay mode captures charged particles produced by the $K^+ \rightarrow \mu^+ + \nu_\mu$ (branching ratio 64 %) and $K^+ \rightarrow \pi^+ + \pi^0$ (branching ratio 21 %) decays. However, it is less efficient than the $p \rightarrow e^+ + \pi^0$ search. However, since the lifetime of K^+ is $\sim$ 12 ns, the background is identified by observing prompt γ rays (6.3 MeV), which are emitted at a rate of about 40% due to nuclear deexcitation after proton decay. The time resolution of the HK photosensor has been improved by a factor of 2 from that of the SK, and the detection efficiency of gamma rays due to deexcitation is expected to be improved. There are three ways to search for $p \rightarrow \bar{\nu} + K^+$ events, focusing on prompt γ, muons, and $\pi^+\pi^0$. In particular, the search for $\pi^+\pi^0$ requires the number of neutron events to be zero, as in the $p \rightarrow e^+ + \pi^0$ search. With such a search, if the lifetime of the $p \rightarrow \bar{\nu} + K^+$ decay is

$\tau_p < 2 \times 10^{34}$ years, the proton decay can be found with a significance of 3σ after 10 years of observation.

In addition to the above two decay modes, the GUT predicts a variety of other decay modes, with different branching ratios depending on the model and parameters. Therefore, it is important to search a wide range of decay modes to understand physics on the grand unified energy scale, and HK is expected to be sensitive to many decay modes. The main proton decay modes and the regions of the lifetimes measurable by the HK experiment are shown in Figure A.12 [30].

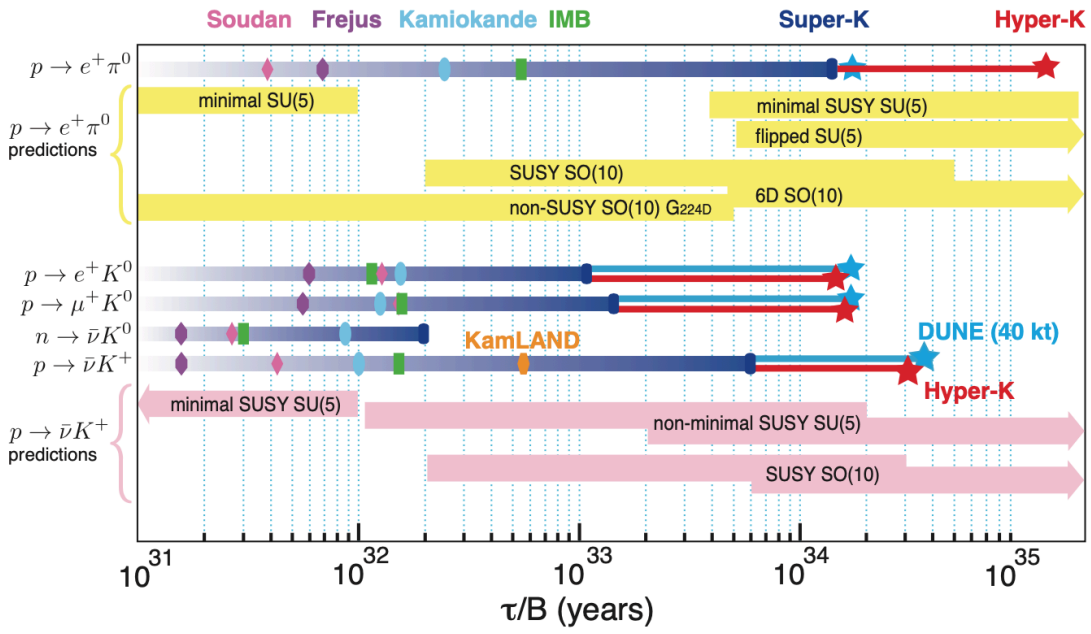

Figure A.5: Theoretical and experimental predictions of the lifetimes of the main proton decay modes and comparison of the predicted values [30]. Experimental results show lifetime limitations of SK and due to earlier experiments. For HK and DUNE, the year measurements show the expected values, indicating that the 10-year observation of HK is sensitive to the life span expected in general.

Appendix B

Convolutional Neural Network for event classification

This chapter summarizes the creation of the Convolutional Neural Network (CNN) for the binary classification of Water Cherenkov detector events.

For this classification, I have created my own CNN based on the example provided by Benoit Cayla [32]. To do this, we'll use Python & TensorFlow 2.x (with keras). As mentioned in Chapter 4, the architecture of such a network is very often based on a stack of convolutional layers, followed by deep, dense layers that do the decision-making. In our case, the layers of our CNN are stacked as follows:

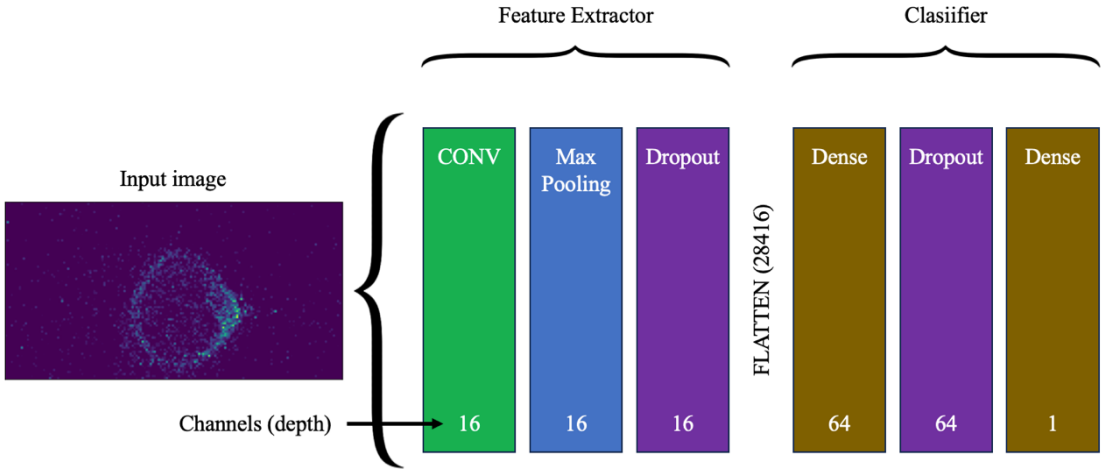

Figure B.1: Convolutional Neural Network layers

A CNN has different types of layers. These include convolution layers. As seen in Figure B.1, we have four different layers in the CNN we have modeled. The first convolution layer is a Conv2D layer and have several parameters: 16 filters, pattern size $(3, 3)$, an activation function. This layer passes over each pixel of the image (strides are set as default at $(1,1)$) to extract patterns of size 3×3 pixels (Figure B.2). The layer performs this action 16 times. With a Conv2D layer, we get 16 feature-maps, 16 image filters, each containing its own characteristics. This is a lot of information. This information is

precious, but the main idea of Machine Learning is to reduce this information to data that can be interpreted by humans. Once we have used a Conv2D layer, we need to reduce the result. This is easily done with the MaxPooling2D layer. Whereas Conv2D extracts features from an image to create feature maps, MaxPooling2D extracts the most important value from each feature map pattern. It has one main parameter: a kernel of size (2,2), the MaxPooling2D layer adapting its filter number to the previous one. The Dense layer is the basic Deep Learning layer. It simply takes an input, and applies a basic transformation with its activation function. The Dense layer is essentially used to modify the dimensions of the tensor. The dropout layer is designed to prevent over-fitting on training data by dropping units in a neural network.

Reminding we start with a 3-dimensional image (height, width, color), a 3D-tensor, and end with a one-dimensional label (a character string), a 1D-tensor, a convolution layer returns a 3D-tensor, a 3-dimensional tensor, so it is the final layer. A layer called Flatten is used to flatten the tensor, reducing its dimension. It takes a 3D-tensor as input and returns a 1D-tensor. The data finally reaches a prediction layer, such as the Dense layer, which provides the label detected by the Deep Learning model.

Note that in the case of this model, Dropout layers were implemented after a first attempt, in order to reduce overfitting during model training.

```
model = models.Sequential()

model.add(layers.Conv2D(16, (3, 3), activation='relu',
                        input_shape=(51, 150, 2)))
model.add(layers.MaxPooling2D((2, 2)))
model.add(layers.Dropout(.3))

model.add(layers.Flatten())
model.add(layers.Dense(64, activation='relu' ))
model.add(layers.Dropout(.3))
model.add(layers.Dense(2))

model.summary()
```

Figure B.2: Python code used to create the CNN for event image classification

After compiling the model, we have:

```
Model: "sequential_7"
_________________________________________________________________
Layer (type)                 Output Shape              Param #
=================================================================
conv2d_7 (Conv2D)            (None, 49, 148, 16)       304
_________________________________________________________________
max_pooling2d_7 (MaxPooling2 (None, 24, 74, 16)        0
_________________________________________________________________
dropout_14 (Dropout)         (None, 24, 74, 16)        0
_________________________________________________________________
flatten_7 (Flatten)          (None, 28416)             0
_________________________________________________________________
dense_13 (Dense)             (None, 64)                1818688
_________________________________________________________________
dropout_15 (Dropout)         (None, 64)                0
_________________________________________________________________
dense_14 (Dense)             (None, 2)                 130
=================================================================
Total params: 1,819,122
Trainable params: 1,819,122
Non-trainable params: 0
_________________________________________________________________
```

We can see that our model will have to learn 1,819,122 parameters, so this will take a few minutes during the training phase.

Bibliography

[1] S. V. Cao, V. N. T. Nguyen, T. Le, and V. T. Tran, *A Roadmap to Build Experimental High Energy Physics at ICISE, Vietnam*, October 4, 2017

[2] Georges Aad, Tatevik Abajyan, B. Abbott, J .Abdallah, S. Abdel Khalek, Ahmed Ali Abdelalim, R. Aben, B. Abi, M. Abolins, OS. AbouZeid, et al. *Observation of a new particle in the search for the Standard Model Higgs boson with the ATLAS detector at the LHC*, 2012.

[3] B.T. Cleveland (Pennsylvania U.), Timothy Daily (Pennsylvania U.), Raymond, Jr. Davis (Pennsylvania U.), James R. Distel (Pennsylvania U.), Kenneth Lande (Pennsylvania U.) et al., *Measurement of the solar electron neutrino flux with the Homestake chlorine detector*, DOI: 10.1086/305343

[4] IceCube collaboration, *IceCube Data for Neutrino Point-Source Searches Years 2008-2018*, arXiv:2101.09836, 2021.

[5] *Nota di Enrico Fermi*. An attempt to a β rays theory.

[6] Clyde L. Cowan Jr., Frederick Reines, FB. Harrison, HW. Kruse, and AD. McGuire. *Detection of the free neutrino: a confirmation*, 1956.

[7] Yoshiyuki Fukuda, T. Hayakawa, E. Ichihara, K. Inoue, K. Ishihara, Hirokazu Ishino, Y. Itow, T. Kajita, J. Kameda, S. Kasuga, et al. *Evidence for oscillation of atmospheric neutrinos*, 1998.

[8] K.A. Olive et al. (Particle Data Group), Chinese Physics C38, 090001, 2014.

[9] KamLAND-Zen Collaboration, A. Gando et al., *Search for Majorana Neutrinos near the Inverted Mass Hierarchy Region with KamLAND-Zen*, arXiv:1605.02889 [hep-ex], 2016.

[10] Particle Data Group, RL. Workman, VD. Burkert, V. Crede, E. Klempt, U. Thoma, L. Tiator, K. Agashe, G. Aielli, BC. Allanach, et al. *Review of particle physics. Progress of theoretical and experimental physics*, 2022.

[11] T. Kajita*, Atmospheric Neutrinos And Discovery Of Neutrino Oscillations*, Proc. Japan, 2010.

[12] M. Honda, T. Kajita, K. Kasahara, and S. Midorikawa, *Improvement of low energy atmospheric neutrino flux calculation using the JAM nuclear interaction model*, 2011.

[13] G. Battistoni, A. Ferrari, T. Montaruli, and P. R. Sala., *The FLUKA atmospheric neutrino flux calculation,* 2003.

[14] G. D. Barr, T. K. Gaisser, P. Lipari, Simon Robbins, and T. Stanev, *A Three-dimensional calculation of atmospheric neutrinos*, 2004.

[15] Y. Fukuda, T. Hayakawa, E. Ichihara, M. Ishitsuka, Y. Itow, et al., *The Super-Kamiokande detector*, 2002.

[16] Y. Suda, *Search for Proton Decay Using an Improved Event Reconstruction Algorithm in Super-Kamiokande*, Ph.D. thesis, University of Tokyo, 2017.

[17] Github: https://github.com/WCSim

[18] Docker: https://www.docker.com

[19] Thomas Dealtry, Alexander Himmel, Johannes Hoppenau, Joseph Lozier, *Simulating Water Cherenkov Detectors Using WCSim*, 2016.

[20] Hyper-Kamiokande Collaboration, *Hyper-Kamiokande*, 2015

[21] M. Jiang et al., *Atmospheric Neutrino Oscillation Analysis with Improved Event Reconstruction in Super-Kamiokande IV*, 2019.

[22] Mo Jia et al., Maximum Likelihood Reconstruction Of Water Cherenkov Events With Deep Generative Neural Networks, arXiv:2202.01276v1, 2022.

[23] Paul BLANC-DURAND, *Réseaux de neurones convolutifs en médecine nucléaire : Applications à la segmentation automatique des tumeurs gliales et à la correction d'atténuation en TEP/IRM*, 2018.

[24] Water Cherenkov Machine Learning: https://github.com/WatChMaL

[25] R. N. Cahn, D. A. Dwyer, S. J. Freedman, W. C. Haxton, R. W. Kadel, Yu. G. Kolomensky, K. B. Luk, P. McDonald, G. D. Orebi Gann, A. W. P. Poon, *White Paper: Measuring the Neutrino Mass Hierarchy*, 2013.

[26] Baran Bodur, Kate Scholberg, $\nu_e - {}^{16}O$ *Interactions with Low Energy Atmospheric Neutrinos in Super-Kamiokande*, 2021.

[27] Masato Shiozawa (UTokyo), *Japan-based neutrino program*, https://www-sk.icrr.u-tokyo.ac.jp/hk/doc/170317-Shiozawa-Hyper-K.pdf, 2017.

[28] *Comprehensive measurement of pp-chain solar neutrinos*. Nature, Vol. 562, No. 7728, pp. 505–510, 2018.

[29] Hans-Thomas Janka, *Neutrino Emission from Supernovae*, arxiv: 1702.08713, 2017.

[30] K. Abe, Ke. Abe, H. Aihara, A. Aimi, R. Akutsu, C. Andreopoulos, I. Anghel, LHV. Anthony, M. Antonova, Y. Ashida, et al. *Hyper-kamiokande design report*, arXiv:1805.04163, 2018.

[31] S. Mine, J. L. Alcaraz, S. Andringa, S. Aoki, J. Argyriades, K. Asakura, R. Ashie, F. Berghaus, H. Berns, H. Bhang, et al., *Experimental study of the atmospheric neutrino backgrounds for* $p \rightarrow e^+ + \pi^0$ *searches in water cherenkov detectors*, 2008.

[32] Benoit Cayla, La data Guide de survie dans le monde de la donnée, Ref. ENI : HSDPDATA, 2022.